Sustainable Synthesis of a Catalytic Active One-Dimensional Lanthanide-Organic Coordination Polymer

Ricardo F. Mendes, Patrícia Silva, Margarida M. Antunes,

Anabela A. Valente, Filipe A. Almeida Paz*

A contribution from

Department of Chemistry, CICECO, University of Aveiro, 3810-193 Aveiro, Portugal

Electronic Supporting Information

To whom correspondence should be addressed:

Filipe A. Almeida Paz
Department of Chemistry, CICECO
University of Aveiro
3810-193 Aveiro
Portugal

E-mail: filipe.paz@ua.pt
FAX: (+351) 234 401470
Telephone: (+351) 234 370200 (Ext. 23553)

Table of Contents

1. Experimental Section

1.1. General Instrumentation

SEM (Scanning Electron Microscopy) images were acquired using either a Hitachi S4100 field emission gun tungsten filament instrument working at 25 kV, or a high-resolution Hitachi SU-70 working at 4 kV. Samples were prepared by deposition on aluminium sample holders followed by carbon coating using an Emitech K950X carbon evaporator. EDS (Energy Dispersive X-ray Spectroscopy) data and SEM mapping images were recorded using the latter microscope working at 15 kV and using either a Bruker Quantax 400 or a Sprit 1.9 EDS microanalysis system.

Thermogravimetric analyses (TGA) were carried out using a Shimadzu TGA 50, from ambient temperature to *ca*. 800 ºC (heating rate of 5 ºC/min), and from ambient temperature to *ca*. 160 ºC (heating rate of 1 ºC/min) under a continuous stream of air or N_2 at a flow rate of 20 mL min^{-1}.

Fourier Transform Infrared (FT-IR) spectra (in the range 4000-350 cm^{-1}) were recorded as KBr pellets (2 mg of sample were mixed in a mortar with 200 mg of KBr) using a Bruker Tensor 27 spectrometer by averaging 256 scans at a maximum resolution of 2 cm^{-1}.

Elemental analyses for C, N and H were performed with a Truspec 630-200-200 elemental analyzer at the Department of Chemistry, University of Aveiro. Samples (with mass typically between 1 and 2 mg) were combusted at 850 ºC for 4 minutes under an oxygen atmosphere. Helium was used as the carrier gas.

Routine Powder X-Ray Diffraction (PXRD) data for all prepared materials were collected at ambient temperature on a Empyrean PANalytical diffractometer (Cu $K_{a1,2}$ X-radiation, λ_1 = 1.540598 Å; λ_2 = 1.544426 Å), equipped with an PIXcel 1D detector and a flat-plate sample holder in a Bragg-Brentano para-focusing optics configuration (45 kV, 40 mA). Intensity data were collected by the step-counting method (step 0.01º), in continuous mode, in the *ca*. $3.5 \leq 2\theta \leq 50º$ range.

Variable-temperature powder X-ray diffraction data were collected on an PANalytical X'Pert Powder diffractometer Cu $K_{a1,2}$ X-radiation (λ_1 = 1.540598 Å; λ_2 = 1.544426 Å), equipped with an PIXcel 1D detector, and a flat-plate sample holder in a Bragg–Brentano para-focusing optics configuration (40 kV, 50 mA), and a high-temperature Anton Paar HKL 16 chamber controlled by an Anton Paar 100 TCU unit. Intensity data were collected in the continuous mode (*ca.* 100 seconds data acquisition) in the angular range *ca.* $3.5 \leq 2\theta° \leq 50$.

^{31}P MAS spectra were recorded at 9.4 T on a Bruker Avance 400 wide-bore spectrometer (DSX model) on a 4 mm BL cross-polarization magic-angle spinning (CPMAS) VTN probe at 161.9 MHz. ^{31}P HPDEC spectra a 90° single pulse excitation of 3.0 μs was employed; recycle delay: 60 s; ν_R= 8 or 12 kHz. Chemical shifts are quoted in parts per million (ppm) with respect to an 85% H_3PO_4 solution.

1.2. Reagents and Solvents

Chemicals, including solvents, were readily available from commercial sources and were used as received without further purification: lanthanum (III) oxide (99.9%, Sigma-Aldrich); nitrilotri(methylphosphonic) acid (≥97.0%, Sigma-Aldrich); sulphuric acid (98%, José Manuel Gomes dos Santos Lda); potassium bromide (KBr for infra-red spectroscopy, BDH SpectrosoL); styrene oxide (C_8H_8O, *purum* ≥97%, Fluka); methanol (Chromasolv for HPLC, ≥99.9%, Sigma-Aldrich); ethanol absolute (analytical grade 99.9%, Scharlau, ACS); benzaldehyde (99%, Sigma-Aldrich).

1.3. Synthesis of $[La_2(H_3nmp)_2(H_2O)_4]\cdot 4.5H_2O$ (1)

1.3.1 Microwave-Assisted Synthesis: 1mw

A reactive mixture composed of 0.1422 g (0.477 mmol) of nitrilotri(methylphosphonic) acid (H_6nmp) and 0.0808 g (0.247 mmol) of La_2O_3 in *ca.* 5 mL of distilled water and 100 μL of concentrated sulphuric acid, with an overall molar ratio of *ca.* 0.5 : 1 : 600 : 4 (La^{3+} : H_6nmp : H_2O : H_2SO_4), was prepared at ambient temperature inside a 10 mL IntelliVent microwave reactor. Reaction took place inside a CEM Focused Microwave Synthesis System Discover S-Class equipment, under constant magnetic stirring (controlled by the microwave equipment) using, typically, an irradiation power of 50 W. A constant flow of air (*ca.* 20-30 psi of pressure) ensured a close control of the temperature inside the reactor. The resulting product, $[La_2(H_3nmp)_2(H_2O)_4]\cdot 4.5H_2O$ (**1mw**), was isolated as a white microcrystalline powder and it was recovered by vacuum filtration, washed with copious amounts of distilled water and then air-dried at ambient temperature.

The optimal synthetic conditions were found by systematically varying the microwave-assisted experimental parameters such as: temperature (60, 100, and 140 ºC) and irradiation time (1, 5, 15 and 30 min). The irradiation power was maintained constant at 50 W.

Elemental CHN composition (%). Calcd: C 6.65; H 3.31, N 2.67. Found: C 6.85; H 3.83, N 2.66.

Thermogravimetric analysis (TGA) data (weight losses in %) and derivative thermogravimetric peaks (DTG; in italics inside the parentheses): 22-99 ºC -5.53% (*82 ºC*); 99-189 ºC -9.41% (*138 ºC*); 189-472 -6.32% (*401 ºC*); 472-554 ºC -1.34% (*509 ºC*); 554-778 ºC -4.75% (*704 ºC*). Total loss: 27.4%.

Selected FT-IR data (in cm^{-1}; from KBr pellets): ν(H_2O) = 3500-3000*br*; ν(−CH_2−) = 3064-2855*w-m*; ν(POH) = 2828-2512*w-m*; δ(H_2O) = 1651*m*; δ(P−CH_2) = 1450*m*, 1431*m* and 1417*m*; ν(P=O) = 1300-1100*m-vs*; ν(P−O) = 1100-873*vs*; ν(P−C) = 791*m* and 754*m*.

1.3.2 Hydrothermal Synthesis: 1h

The hydrothermal approach towards **1h** is similar to that describe above for **1mw** with very small modifications: a reactive mixture containing H_6nmp (0.26 g, 0.869 mmol) and La_2O_3 (0.14 g, 0.430

mmol) in *ca.* 10.0 mL of distilled water, molar ratio 1 : 2 : 1300 (La^{3+} : H_6nmp : H_2O), but without the addition of acid, was placed inside an adapted Teflon-lined Parr Instruments reaction vessel (autoclave with internal volume of *ca.* 10 mL). The vessel was then placed inside a pre-heated oven at 100 ºC for a period of 72 hours. After this period, the vessel was quenched to ambient temperature by immersing under cool water. The resulting white powder, identified as **1h**, was recovered by vacuum filtration, washed with copious amounts of distilled water and then air-dried at ambient temperature.

Elemental CHN composition (%). Calcd: C 6.65; H 3.31, N 2.67. Found: C 6.73; H 3.68, N 2.54.

Thermogravimetric analysis (TGA) data (weight losses in %) and derivative thermogravimetric peaks (DTG; in italics inside the parentheses): 22-31 ºC -0.62% (*28 ºC*); 31-80 ºC -4.82% (*73 ºC*); 80-105 -3.36% (*91 ºC*); 105-160 ºC -7.11% (*125 ºC*); 160-434 ºC -3.35% (*301 ºC*); 434-512 ºC -1.88% (*466 ºC*); 512-787 -6.23 ºC (*543 ºC*). Total loss: 27.4%.

Selected FT-IR data (in cm^{-1}; from KBr pellets): ν(H_2O) = 3500-3125; ν(−CH_2−) = 3055-2915*w-m*; ν(POH) = 2844-2530*w-m*; δ(H_2O) = 1664*m*; δ(P−CH_2) = 1450*m*, 1431*m* and 1417*m*; ν(P=O) = 1255-1109*m-vs*; ν(P−O) = 1109-888*vs*; ν(P−C) = 755*m* and 727*m*.

1.3.3 One-pot synthesis: 1op

This approach was developed and optimized with two main objectives: i) to isolate crystals suitable for single-crystal X-ray diffraction studies; ii) to develop an alternative sustainable synthetic approach to that described above where microwave irradiation was used. A reactive mixture composed of 0.0845 g (0.283 mmol) of nitrilotri(methylphosphonic) acid (H_6nmp) and 0.1588 g (0.487 mmol) of La_2O_3 in *ca.* 10 mL of distilled water, with an overall molar ratio of *ca.* 0.5 : 1 : 2000 (La^{3+} : H_6nmp : H_2O), was prepared at ambient temperature inside a 25 mL round glass flask and kept under vigorous magnetic stirring for 4 hours at 120 ºC. The resulting white powder was recovered by vacuum filtration, washed with copious amounts of distilled water and then air-dried at ambient temperature.

Elemental CHN composition (%). Calcd: C 6.65; H 3.31, N 2.67. Found: C 6.62; H 3.47, N 2.70.

Thermogravimetric analysis (TGA) data (weight losses in %) and derivative thermogravimetric peaks (DTG; in italics inside the parentheses): 22-45 ºC -1.62% (*34 ºC*); 45–96 ºC -4.65% (*75 ºC*); 96-180 -9.17% (*128 ºC*); 180 –458 ºC -5.53% (*402 ºC*); 458–771 ºC -4.46% (*724 ºC*). Total loss: 25.4%.

Selected FT-IR data (in cm^{-1}; from KBr pellets): ν(H_2O) = 3500-3125; ν(−CH_2−) = 3055-2915*w-m*; ν(POH) = 2844-2530*w-m*; δ(H_2O) = 1664*m*; δ(P−CH_2) = 1450*m*, 1431*m* and 1417*m*; ν(P=O) = 1255-1109*m-vs*; ν(P−O) = 1109-888*vs*; ν(P−C) = 755*m* and 727*m*.

1.4. Stability Tests of $[La_2(H_3nmp)_2(H_2O)_4]\cdot 4.5H_2O$ (1mw)

The bulk $[La_2(H_3nmp)_2(H_2O)_4]\cdot 4.5H_2O$ (**1mw**) material was subjected to both acidic and basic conditions. Typically, 20 mg of **1mw** was placed in 5mL of distilled water under vigorous magnetic stirring. Different quantities of HCl 6M, concentrated sulphuric acid or NaOH 1M (50, 100, 200, 500 and 1000 μL) were added dropwise, and the resulting mixture was left under magnetic stirring for a period of 24 h at ambient temperature. After this period, the remaining material was filtered, washed with copious amount of water, and dried in open air. Structural integrity of the materials was assessed using powder X-ray diffraction studies.

1.6. Transformation Tests

1.6.1 Hydrothermal conditions

In a Teflon-lined Parr Instruments reaction vessel *ca.* 30 mg of $[La_2(H_3nmp)_2(H_2O)_4]\cdot 4.5H_2O$ (**1mw**) were mixed with 4 mL of distilled water and 1 mL of hydrochloric acid 6 M. The vessel was allowed to heat up to *ca.* 100 ºC and the reaction took place over a period of 24 h, followed by a slow cooling of the vessel up to ambient temperature (over a period of 48 h). The remaining solid was recovered by vacuum filtration, washed with distilled water and dried in open air. The resulting product was identified as a pure phase identical to $[La(H_3nmp)]\cdot 1.5H_2O$ (**2**), previously reported by our group by Cunha-Silva *et al.*[1]

Using a similar experimental procedure to that described in the previous paragraph but using instead 48 h of reaction followed by a quenching of the reaction vessel in cool water, **1mw** was found to be converted into a mixture of $[La(H_3nmp)]\cdot 1.5H_2O$ (**2**)[1] and $[La(H_3nmp)]$ (**3**),[2] with the latter material being the predominant phase.

1.6.2 One-pot

In this experiment *ca.* 30 mg of **1mw** was mixed with 4.5 mL of distilled water and 0.5 mL of hydrochloric acid 6 M in a round flask under vigorous magnetic stirring at 100 ºC. Samples were removed at different reaction times (1, 5, 6, 7, 8 and 24 hours), filtered and washed with copious amounts of water. Phase identification was performed using powder X-ray diffraction studies, showing that **1mw** was fully converted into pure $[La(H_3nmp)]\cdot 1.5H_2O$ (**2**).[1]

1.7. Single-Crystal X-ray Diffraction Studies: $[La_2(H_3nmp)_2(H_2O)_4]\cdot 4.5H_2O$ (1op)

Inspection of various batches of the microcrystalline powder isolated from the one-pot synthesis approach was performed using a Stemi 2000 stereomicroscope equipped with Carl Zeiss lenses. This allowed the identification of a rare, larger colourless block (even though the dimensions are only of about

0.08×0.06×0.01 mm) which was investigated using single-crystal X-ray diffraction. This unique block was manually selected and harvested from the batch powder and immersed in highly viscous FOMBLIN Y perfluoropolyether vacuum oil (LVAC 140/13, Sigma-Aldrich).[3] The crystal was then mounted on a Hampton Research CryoLoop and preliminary X-ray diffraction data were collected at 180(2) K on a Bruker D8 QUEST equipped with Mo Kα sealed tube (λ = 0.71073 Å), a multilayer TRIUMPH X-ray mirror, a PHOTON 100 CMOS detector, and a Oxford Instruments Cryostrem 700+ Series low temperature device. The instrument was controlled with the APEX2 software package.[4]

Unit cell indexation using the algorithm implemented in the APEX2 software package did not allow a sensible unit cell identification, mainly because of the presence of various crystal domains and an overall weak diffraction. Figure S1A shows one diffraction image from each of the final performed runs emphasising the weak nature of the diffraction observed from the selected, very small crystallite. Indexation and the calculation of the proper orientation matrix could only be achieved by using data from synchrotron X-ray powder diffraction studies (see the following sections for additional details) in conjunction with the CELL_NOW command prompt software package: in short, the unit cell search was restricted to narrow values for the cell parameters using as starting premise the data from cell indexation using TOPAS-Academic V5.[5]

Using the monoclinic unit cell derived from synchrotron studies the APEX2 software package calculated a 4-run data collection strategy composed of ω and φ scans. The collected data set was processed using the latest integrated plug-in in the controlling software package (SAINT+),[6] and corrected for absorption by the multiscan semi-empirical method implemented in SADABS.[7]

The crystal structure of $[La_2(H_3nmp)_2(H_2O)_4]\cdot 4.5H_2O$ (**1op**) was solved using the algorithm implemented in SHELXT-2014,[8] which allowed the immediate location of almost all of the heaviest atoms composing the molecular unit of the two compounds. The remaining missing non-hydrogen atoms were located from difference Fourier maps calculated from successive full-matrix least-squares refinement cycles on F^2 using the latest SHELXL from the 2014 release.[9]

In general, all non-hydrogen atoms were refined using anisotropic displacement parameters, particularly those composing the one-dimensional neutral hybrid $_\infty^1[La_2(H_3nmp)_2(H_2O)_4]$ polymer. Besides the four coordinated water molecules, 4.5 additional solvent molecules were located in the void spaces of the crystal distributed among six independent crystallographic locations. These uncoordinated solvent molecules were included in the final structural model with isotropic displacement parameters, one for each chemical moiety.

Hydrogen atoms bound to carbon and nitrogen were placed at their idealized positions using the *HFIX 23* or *HFIX 13* in SHELXL-2014. All hydrogen atoms were included in subsequent refinement cycles with isotropic thermal displacements parameters (U_{iso}) fixed at 1.2×U_{eq} of the parent atoms. Hydrogen atoms associated with the water molecules, both of crystallization and coordinated to La^{3+},

could not be located from difference Fourier maps and no attempts were made to place them in calculated positions. These atoms were, however, included in the empirical formula of the compound (Table S1). Hydrogen atoms associated with the terminal P-OH groups were placed in calculated positions using the *HFIX 147* instruction in SHELXL-2014. To find which groups should be protonated it was necessary to simultaneously take into account the P-O bond lengths and the possibility of forming hydrogen bonds with neighbouring moieties. These hydrogen atoms were refined by assuming isotropic thermal displacements parameters (U_{iso}) fixed at $1.5 \times U_{eq}$ of the parent oxygen atoms.

The last difference Fourier map synthesis showed for **1op**, the highest peak (1.318 eÅ^{-3}) and the deepest hole (-1.071 eÅ^{-3}) located at 1.16 and 1.42 Å from La2 and H3b, respectively.

All structural refinements were performed using the graphical interface ShelXle.[10] Structural drawings have been created using the software package Crystal Impact Diamond.[11] Information concerning crystallographic data collection and structure refinement details is summarized in Table S1. Tables S2 and S3 gather the most significant geometrical parameters of the two crystallographically independent La^{3+} coordination spheres.

Crystallographic data (including structure factors) for the crystal structure of compound **1op** have been deposited with the Cambridge Crystallographic Data Centre as supplementary publication data No. CCDC-1040381. Copies of the data can be obtained free of charge on application to CCDC, 12 Union Road, Cambridge CB2 2EZ, U.K. FAX: (+44) 1223 336033. E-mail: deposit@ccdc.cam.ac.uk.

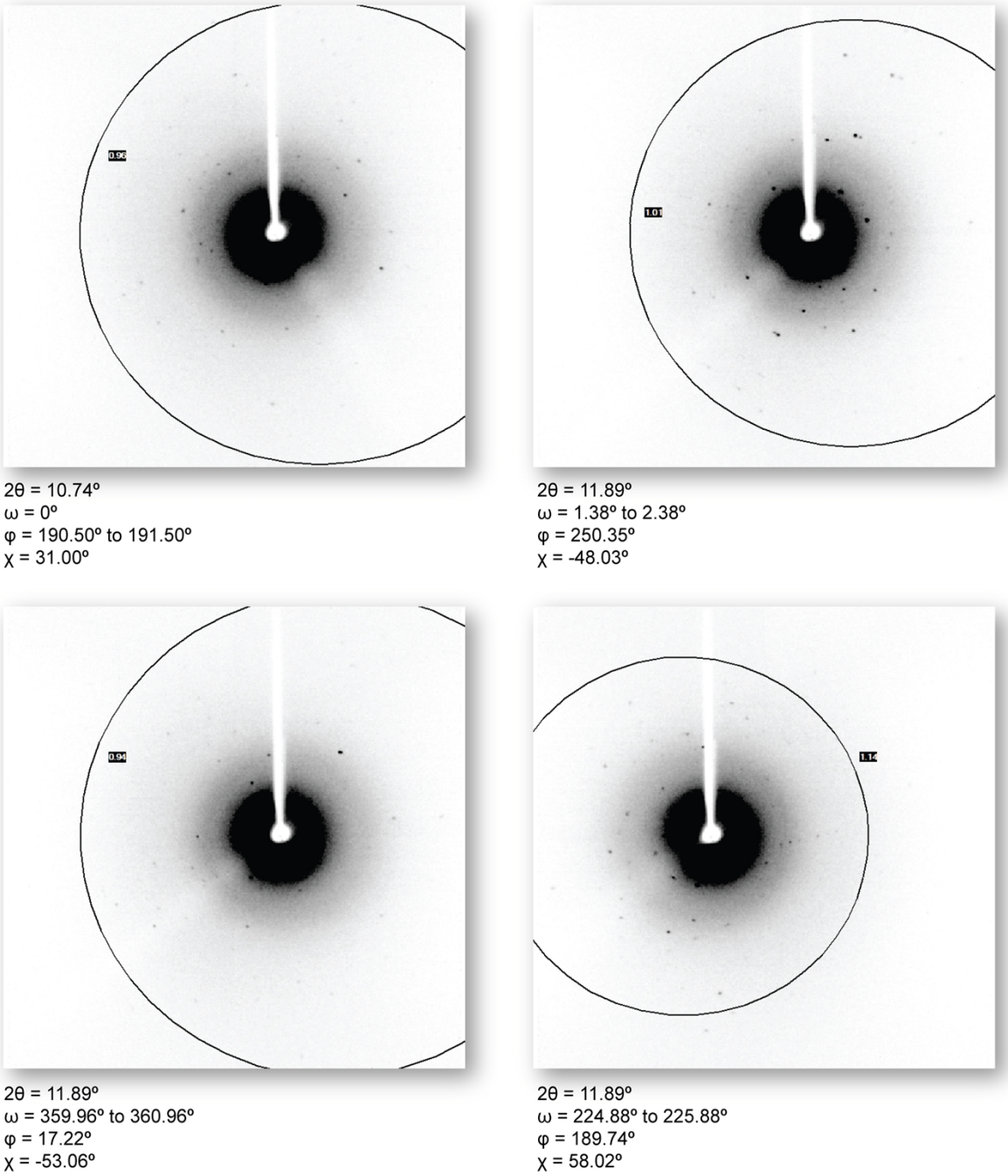

Figure S1A. Selected X-ray diffraction frames from the data collection of the crystal structure of $[La_2(H_3nmp)_2(H_2O)_4]\cdot 4.5H_2O$ (**1op**) showing the poor diffracting capabilities of the small selected crystal. As emphasized, reflections are barely observed above the background for a resolution greater than *ca.* 1 Å.

Table S1. Crystal and structure refinement data for compound $[La_2(H_3nmp)_2(H_2O)_4]\cdot 4.5H_2O$ (**1op**).

Formula	$C_{12}H_{78}La_4N_4O_{53}P_{12}$
Formula weight	2054.06
Crystal system	Monoclinic
Space group	$P2_1/c$
a/Å	14.274(4)
b/Å	18.624(5)
c/Å	12.530(4)
β / º	115.140(12)
Volume/Å^3	3015.3(16)
Z	2
D_c/g cm^{-3}	2.262
μ(Mo-Kα)/mm^{-1}	3.217
Crystal size/mm	0.08×0.06×0.01
Crystal type	Colourless blocks
θ range	3.59 to 25.35
Index ranges	$-17 \le h \le 17$
	$-22 \le k \le 22$
	$-15 \le l \le 15$
Reflections collected	42667
Independent reflections	5510 [R_{int} = 0.2947]
Completeness to θ = 25.24º	99.6%
Final R indices [I>2σ(I)][a,b]	$R1$ = 0.0754
	$wR2$ = 0.1177
Final R indices (all data)[a,b]	$R1$ = 0.1757
	$wR2$ = 0.1464
Weighting scheme[c]	m = 0.0381
	n = 21.7999
Largest diff. peak and hole	1.318 and -1.071 eÅ^{-3}

[a] $R1 = \sum \left| |F_o| - |F_c| \right| / \sum |F_o|$

[b] $wR2 = \sqrt{\sum \left[w\left(F_o^2 - F_c^2\right)^2 \right] / \sum \left[w\left(F_o^2\right)^2 \right]}$

[c] $w = 1/\left[\sigma^2\left(F_o^2\right) + \left(mP\right)^2 + nP \right]$ where $P = \left(F_o^2 + 2F_c^2\right)/3$

Table S2. Selected bond lengths (in Å) and angles (in degrees) for the La1 metal coordination environment present in the single-crystal structure determination of $[La_2(H_3nmp)_2(H_2O)_4]\cdot 4.5H_2O$ (**1op**).[a]

La1–O1	2.400(9)	La1–O14	2.642(9)
La1–O4	2.532(8)	La1–O14^{i}	2.492(8)
La1–O10	2.534(9)	La1–O1W	2.693(9)
La1–O11^{i}	2.429(9)	La1–O2W	2.699(10)
La1–O13	2.733(9)		
O1–La1–O4	75.7(3)	O11^{i}–La1–O10	140.1(3)
O1–La1–O10	72.1(3)	O11^{i}–La1–O13	99.0(3)
O1–La1–O11^{i}	128.3(3)	O11^{i}–La1–O14	74.2(3)
O1–La1–O13	132.6(3)	O11^{i}–La1–O14^{i}	73.2(3)
O1–La1–O14	134.3(3)	O11^{i}–La1–O1W	65.8(3)
O1–La1–O14^{i}	79.6(3)	O11^{i}–La1–O2W	71.8(3)
O1–La1–O1W	114.6(3)	O14–La1–O13	53.8(3)
O1–La1–O2W	63.2(3)	O14–La1–O1W	111.0(3)
O4–La1–O10	77.6(3)	O14–La1–O2W	142.8(3)
O4–La1–O13	66.8(3)	O14^{i}–La1–O4	150.2(3)
O4–La1–O14	118.0(3)	O14^{i}–La1–O10	79.1(3)
O4–La1–O1W	70.6(3)	O14^{i}–La1–O13	122.4(3)
O4–La1–O2W	97.1(3)	O14^{i}–La1–O14	69.7(3)
O10–La1–O13	72.3(3)	O14^{i}–La1–O1W	136.3(3)
O10–La1–O14	69.5(3)	O14^{i}–La1–O2W	86.4(3)
O10–La1–O1W	143.9(3)	O1W–La1–O13	79.6(3)
O10–La1–O2W	134.8(3)	O1W–La1–O2W	67.4(3)
O11^{i}–La1–O4	136.0(3)	O2W–La1–O13	146.7(3)

[a] Symmetry transformations used to generate equivalent atoms: (i) 1-*x*, 1-*y*, 1-*z*.

Table S3. Selected bond lengths (in Å) and angles (in degrees) for the La2 metal coordination environment present in the single-crystal structure determination of $[La_2(H_3nmp)_2(H_2O)_4]\cdot 4.5H_2O$ (**1op**).[a]

La2–O4	2.685(9)	La2–O13	2.524(9)
La2–O5	2.647(9)	La2–O16	2.458(11)
La2–O5^{ii}	2.475(8)	La2–O3W	2.682(10)
La2–O7	2.573(8)	La2–O4W	2.601(10)
La2–O8^{ii}	2.493(9)		
O5–La2–O4	54.4(3)	O8^{ii}–La2–O4W	70.2(3)
O5–La2–O3W	104.9(3)	O13–La2–O4	67.7(3)
O5^{ii}–La2–O4	120.6(3)	O13–La2–O5	120.8(3)
O5^{ii}–La2–O5	68.0(4)	O13–La2–O7	80.7(3)
O5^{ii}–La2–O7	78.3(3)	O13–La2–O3W	71.7(3)
O5^{ii}–La2–O13	152.4(3)	O13–La2–O4W	93.7(3)
O5^{ii}–La2–O8^{ii}	72.7(3)	O16–La2–O4	131.1(3)
O5^{ii}–La2–O3W	134.1(3)	O16–La2–O5	133.7(3)
O5^{ii}–La2–O4W	89.7(3)	O16–La2–O7	71.2(3)
O7–La2–O4	70.7(3)	O16–La2–O13	77.0(3)
O7–La2–O5	70.6(3)	O16–La2–O3W	121.4(3)
O7–La2–O3W	144.6(3)	O16–La2–O4W	66.2(3)
O7–La2–O4W	137.2(3)	O16–La2–O5^{ii}	79.4(3)
O8^{ii}–La2–O4	101.2(3)	O16–La2–O8^{ii}	127.7(3)
O8^{ii}–La2–O5	73.2(3)	O3W–La2–O4	78.4(3)
O8^{ii}–La2–O7	140.0(3)	O4W–La2–O4	145.4(3)
O8^{ii}–La2–O13	133.9(3)	O4W–La2–O5	141.5(3)
O8^{ii}–La2–O3W	62.2(3)	O4W–La2–O3W	67.8(4)

[a] Symmetry transformations used to generate equivalent atoms: (ii) -*x*, 1-*y*, 1-*z*.

1.8. Synchrotron Powder X-ray Diffraction Studies

High-resolution powder synchrotron X-ray diffraction data for $[La_2(H_3nmp)_2(H_2O)_4]\cdot 4.5H_2O$ (**1mw**) and $[La_2(H_3nmp)_2(H_2O)_4]\cdot 4.5H_2O$ (**1h**) were collected at low temperature (100 K; cooling device from Oxford Instruments) on the powder diffractometer instrument assembled in either the recent ID22 or the ID31 beam line,[12] respectively, at the European Synchrotron Radiation Facility (ESRF), Grenoble, France. The beam lines receive X-rays from the synchrotron source, operating with an average energy of 6 GeV and a current beam of typically 200 mA, from an undulator device. The high signal-to-noise ratio of the data is due to the high brilliance of the synchrotron beam in combination with a Si (111) crystal multi-analyser.

The monochromatic wavelengths were fixed at 0.495958(7) or 0.39981(1) Å for ID22 or ID31, respectively, and calibrated against the Si standard NIST 640c [certified cell parameter a = 5.4311946(92) Å]. Hard X-rays were selected for data collection of both compounds in order to significantly reduce radiation damage, an occurrence observed in previous investigations using related materials but in different experimental conditions. Nevertheless, even at low temperature, the high brilliance of the synchrotron source led to visible damage on the samples. To minimize such effects consecutive data collections were performed on fresh portions of the sample by translating the capillary by *ca.* 1.3 mm.

Fine powdered samples of **1mw** and **1h** were placed inside a Hilgenberg borosilicate glass capillary (*ca.* 0.9 mm of diameter) which was spun during data collection to improve powder averaging over the individual crystallites, ultimately removing eventual textural effects such as preferential orientation. Data were collected in continuous mode with accumulation times increasing with the scattering angle. The counts of the six detectors (covering roughly 5.5º 2θ) were rebinned and normalised to give the equivalent step scans (0.002º) suitable for further structural analyses.

The collected high-resolution powder X-ray diffraction patterns were indexed using the LSI-Index algorithm implemented in TOPAS-Academic V5,[5] and a whole-powder-pattern Pawley fit permitted to unequivocally confirm the monoclinic $P2_1/c$ space group as the most suitable for both compounds, in good agreement with the single-crystal structure determination.

Rietveld structural refinements[13] for both **1mw** and **1h** used as started premise the atomic coordinates and model refined for the compound **1op**. Calculations were performed with TOPAS-Academic V5[14] using a Chebychev polynomial throughout the entire angular range to model the background contribution. The peak shapes for the powder pattern were described using the fundamental parameters approach,[15] with the preferential orientation effects being modelled using a March-Dollase model along the (011) pole.[16] Table S4 gathers all the details pertaining to the ID22 and ID31 synchrotron X-ray data collection, crystal data and structure refinement details for both $[La_2(H_3nmp)_2(H_2O)_4]\cdot 4.5H_2O$ (**1mw**) and $[La_2(H_3nmp)_2(H_2O)_4]\cdot 4.5H_2O$ (**1h**).

Table S4. X-ray data collection, crystal data and structure refinement details for $[La_2(H_3nmp)_2(H_2O)_4]\cdot 4.5H_2O$ (**1mw**) and $[La_2(H_3nmp)_2(H_2O)_4]\cdot 4.5H_2O$ (**1h**).

	1mw	**1h**
Data Collection		
Diffractometer	ID22 beam line – ESRF, France	ID31 beam line – ESRF, France
Wavelength (Å)	0.495958(7)	0.39981(1)
Temperature (K)	100	100
Geometry	Debye-Scherrer	Debye-Scherrer
2θ range (º)	2.000 to 20.000	1.500 to 16.000
Unit Cell		
Formula	$C_{12}H_{44}La_4N_4O_{53}P_{12}$	$C_{12}H_{44}La_4N_4O_{53}P_{12}$
Crystal system	Monoclinic	Monoclinic
Space group	$P2_1/c$	$P2_1/c$
a/Å	14.344(4)	14.3310(4)
b/Å	18.558(5)	18.5148(6)
c/Å	12.468(4)	12.4607(4)
β/º	115.3872(13)	115.526(3)
Volume/Å^3	2998.5(15)	2983.53(17)
Z	2	2
D_c/g cm^{-3}	2.246(1)	2.257(1)
Profile parameters		
Profile function	Fundamental parameters approach	Fundamental parameters approach
Zero shift [2θº]	0.008(23)	0.004(96)
Refinement details		
No. of independent reflections	1162	1154
No. of global refined parameters	189	163
Reliability Factors for data points with Bragg contribution (conventional – not corrected for background)		
R_p	10.29	3.70
R_{wp}	13.50	5.39
R_{exp}	0.95	1.18
GOF	14.17	4.56
Structure Reliability Factors		
R_{Bragg}	4.80	1.55

$$R_p = \frac{\sum_i |y_{i,o} - y_{i,c}|}{\sum_i |y_{i,o}|};\ R_{wp} = \sqrt{\frac{\sum_i w_i (y_{i,o} - y_{i,c})^2}{\sum_i w_i (y_{i,o})^2}};\ R_{Bragg} = \frac{\sum_n |I_{n,o} - I_{n,c}|}{\sum_n I_{n,o}};$$

$$R_{exp} = \sqrt{\frac{(n-p)}{\sum_i w_i (y_{i,o})^2}};\ GOF = \frac{R_{wp}}{R_{exp}}$$

where $y_{i,o}$ and $y_{i,c}$ are the observed and calculated profile intensities, $I_{n,o}$ and $I_{n,c}$ the observed and calculated intensities, respectively. The summations run over *i* data points or *n* independent reflections. Statistical weights w_i are usually taken as $1/y_{i,o}$.

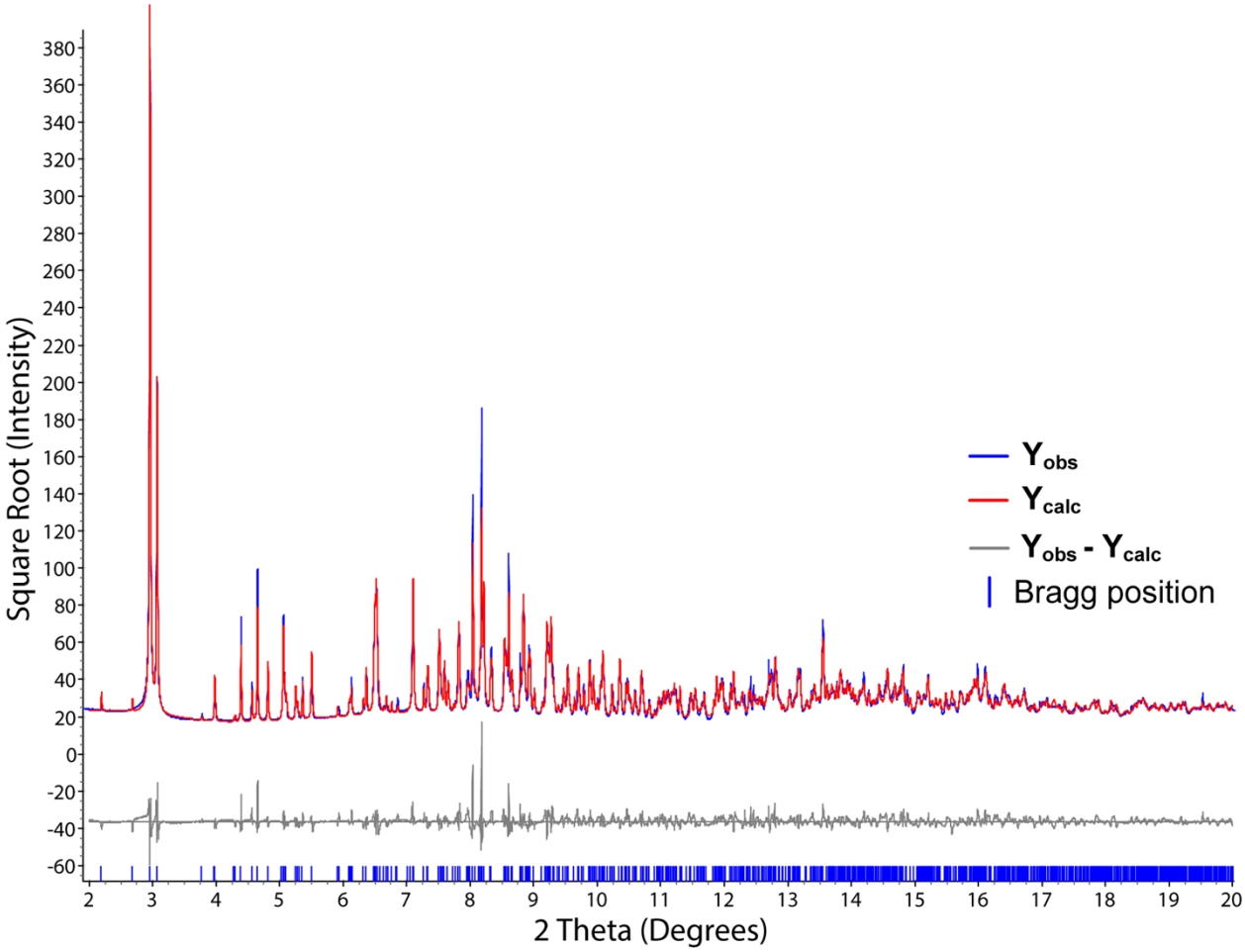

Figure S1B - Final Rietveld plot (synchrotron X-ray diffraction data from ID22 beam line at the ESRF – Grenoble, France) of $[La_2(H_3nmp)_2(H_2O)_4]\cdot 4.5H_2O$ (**1mw**). Observed data points are indicated as a blue line, the best fit profile (upper trace) and the difference pattern (lower trace) are drawn as solid red and grey lines, respectively. Blue vertical bars indicate the angular positions of the allowed Bragg reflections. Refinement details are given in Table S4.

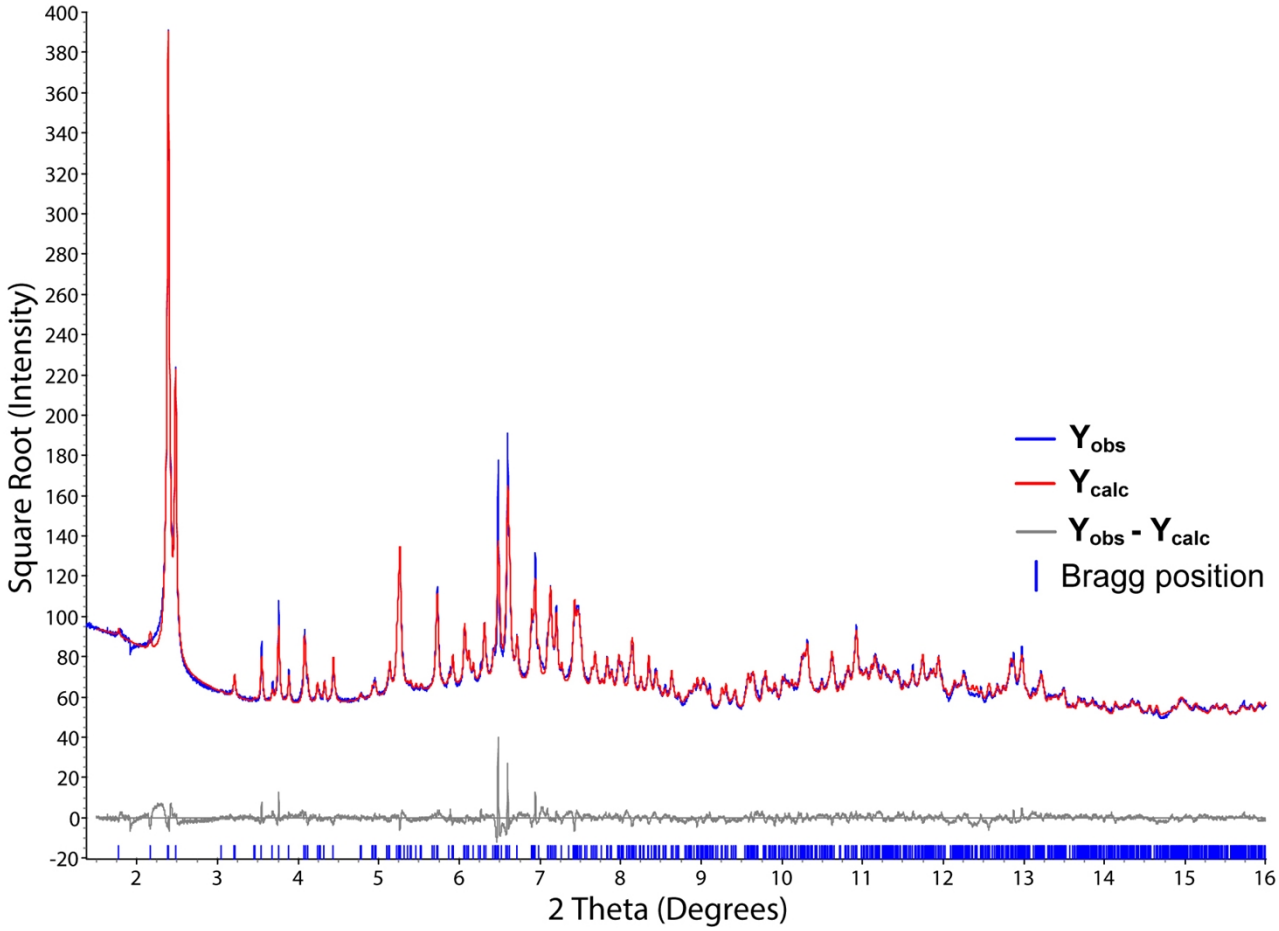

Figure S1C - Final Rietveld plot (synchrotron X-ray diffraction data from ID31 beam line at the ESRF – Grenoble, France) of $[La_2(H_3nmp)_2(H_2O)_4]\cdot 4.5H_2O$ (**1h**). Observed data points are indicated as a blue line, the best fit profile (upper trace) and the difference pattern (lower trace) are drawn as solid red and grey lines, respectively. Blue vertical bars indicate the angular positions of the allowed Bragg reflections. Refinement details are given in Table S4.

1.9. Heterogeneous Catalysis

A 5 mL borosilicate batch reactor, equipped with a magnetic stirrer (800 rpm) and a valve for sampling, was charged with 1.5 mL of methanol or ethanol, 0.4 M of the substrate (styrene oxide – PhEtO - or benzaldehyde - BA) and the catalyst. The catalysts employed in the present work were: $[La_2(H_3nmp)_2(H_2O)_4]\cdot 4.5H_2O$ (**1mw)** (3.3-20 g^1 L^{-1}) and the primary building blocks of the hybrid material, the organic ligand (H_6nmp - $NC_3H_6(PO_3H_2)_3$) and the lanthanide precursor La_2O_3 (3.3 mM). Reactions were carried out under atmospheric air, with the batch reactors immersed in an external thermostated oil bath (35 ºC). Prior to reuse, the solid catalyst **1mw** was separated from the reaction mixture by centrifugation at 3500 rpm, washed with methanol and dried under atmospheric conditions.

The leaching test was carried out for **1mw** by heating a stirred suspension of the hybrid material (3.3 g_1 L^{-1}) in methanol and PhEtO (0.4 M), for 15 min at 35 ºC, and subsequently filtering the solid at the same temperature through a 0.20 μm PVDF w/ GMF Whatman membrane. The obtained filtrate was transferred to a pre-heated (35 ºC) batch reactor and left to react at the same temperature under constant stirring. For comparison, the reaction of PhEtO was also carried in the presence of ethanol under the same experimental conditions.

The progress of the catalytic reactions was monitored using a Varian 3800 GC equipped with a capillary column (Chrompack, CP-SIL 5 CB, 50 m x 0.32 mm x 0.5 mm) and a flame ionization detector. Hydrogen was used as the carrier gas. The identification of the reaction products was carried out by GC-MS (Trace GC 2000 Series (Thermo Quest CE Instruments) - DSQ II (Thermo Scientific)), using He as the carrier gas.

2. Structural Studies

2.1. 1mw

2.1.1. Electron Microscopy Studies: EDS Mapping

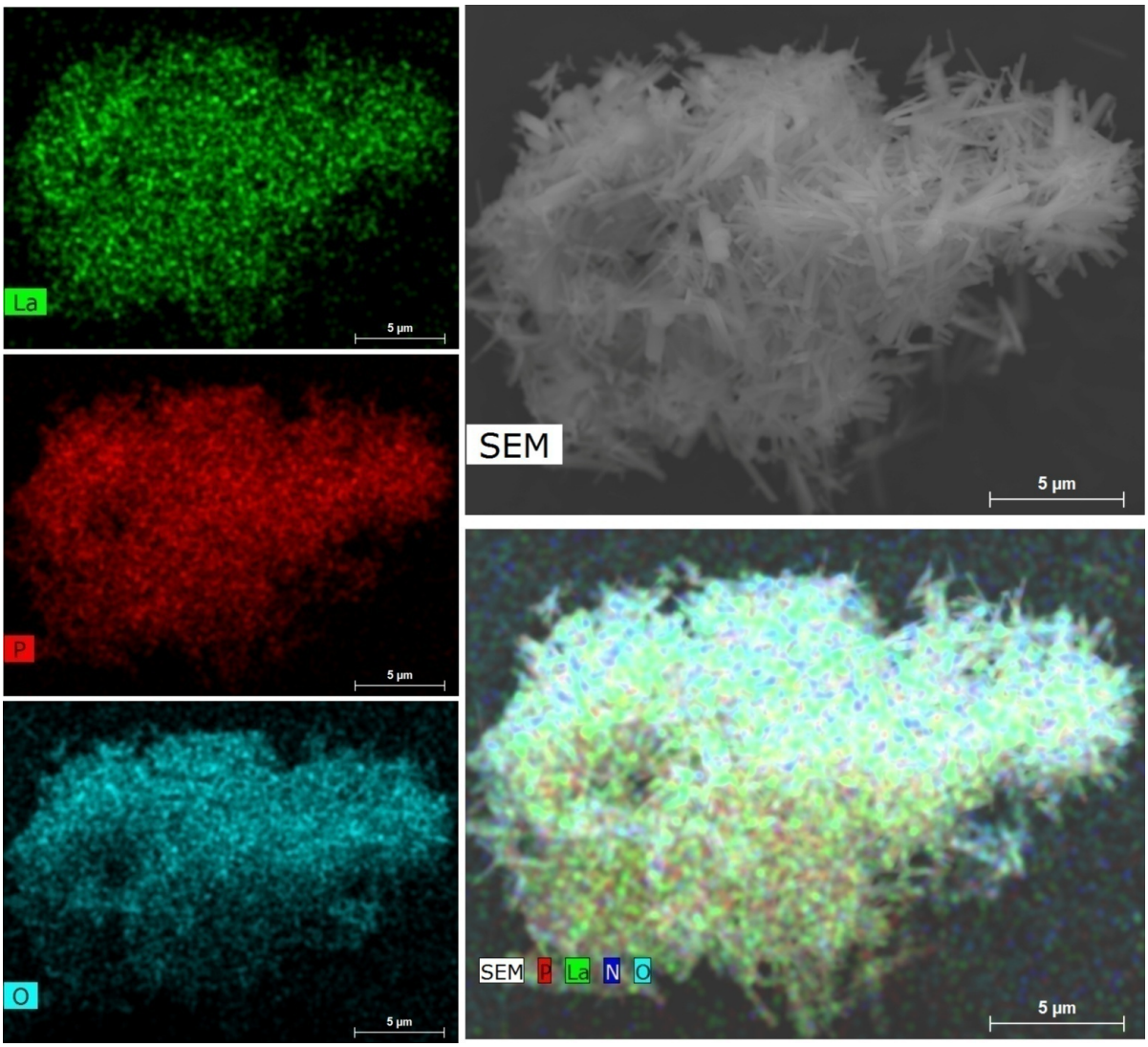

Figure S2. Electron microscopy EDS mapping studies of a representative portion of the $[La_2(H_3nmp)_2(H_2O)_4]\cdot 4.5H_2O$ (**1mw**) bulk material.

Electron microscopy studies on the bulk $[La_2(H_3nmp)_2(H_2O)_4]\cdot 4.5H_2O$ (**1mw**) material reveal that the material is uniformly composed of very thin (*i.e.*, nanometer size in at least one direction) needle-like crystallites with length up to 10 µm (Figure S2). EDS mapping studies show a uniform distribution of the heaviest elements among the bulk sample, ultimately evidencing the presence of a pure phase, as also revealed from the performed X-ray diffraction and solid-state NMR studies.

2.1.2. ^{31}P Solid-State Nuclear Magnetic Resonance

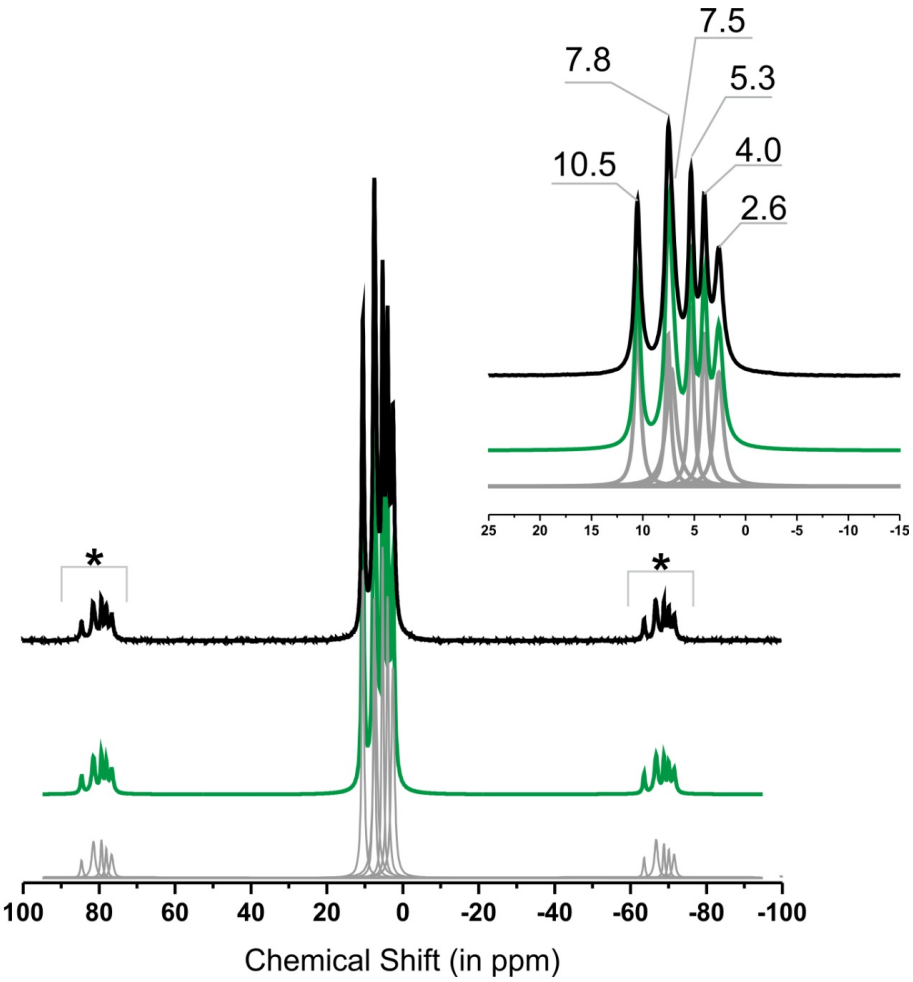

Figure S3. ^{31}P HPDEC MAS spectrum of $[La_2(H_3nmp)_2(H_2O)_4]\cdot 4.5H_2O$ (**1mw**). Spinning sidebands are denoted using an asterisk. Peak deconvolution and integration throughout the entire spectral range (*i.e.*, including the spinning sidebands) gives a ratio of *ca.* 0.89 : 1.16 : 1.25 : 0.88 : 0.86 : 0.96 for the isotropic resonances at *ca.* 10.5, 7.8, 7.5, 5.3, 4.0 and 2.6 ppm, respectively. The green line depicts the overall (*i.e.*, sum) data fit while the individual grey lines correspond to the fits of each single peaks.

The presence of diamagnetic La^{3+} metallic centers in the structure of **1mw** permitted the use of solid-state NMR techniques to probe the composition of the asymmetric unit. Due to the overall poor crystal quality, as described in the technical section dedicated to X-ray diffraction, this solid-state NMR data was of crucial importance to unequivocally assess the number of crystallographically independent organic ligands in the asymmetric unit.

The HPDEC ^{31}P MAS spectrum of **1mw** shows, in the isotropic region, five well-resolved sharp peaks centered at *ca.* 2.6, 4.0, 5.3, 7.5 and 10.5 ppm (Figure S3). One of the resonances has a small visible shoulder, which is more noticeable in the spinning sidebands, referring to a 6th resonance centred at *ca.* 7.8 ppm. In short, the existence of six crystallographically independent phosphorus sites agrees well with the selected space group and the undertaken X-ray crystallographic studies.

2.1.3. Thermogravimetry and Thermodiffractometry

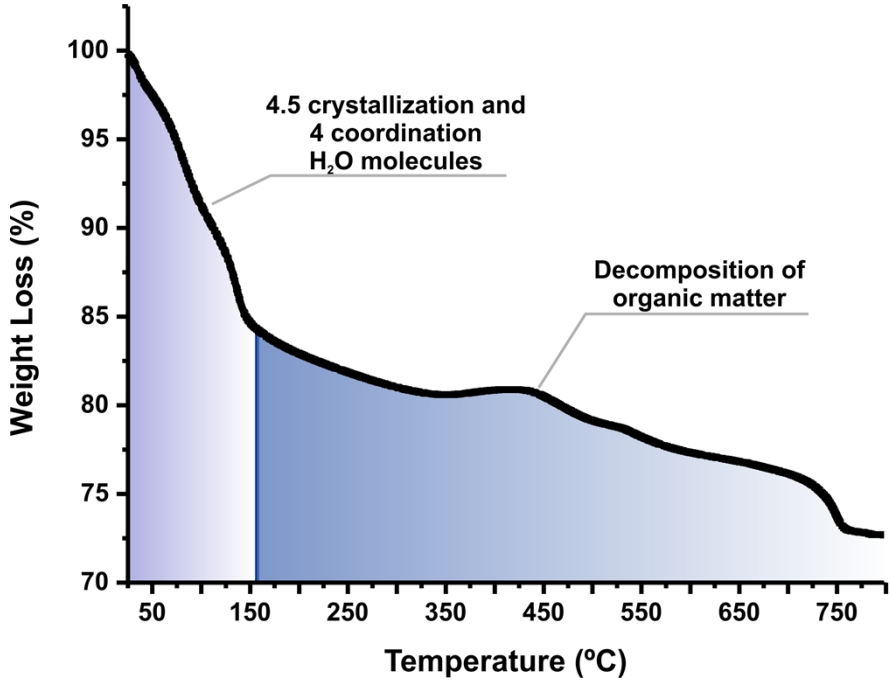

Figure S4. Thermogram of $[La_2(H_3nmp)_2(H_2O)_4]\cdot 4.5H_2O$ (**1h**) collected between ambient temperature and *ca.* 800 ºC with a heating rate of 5 ºC/min.

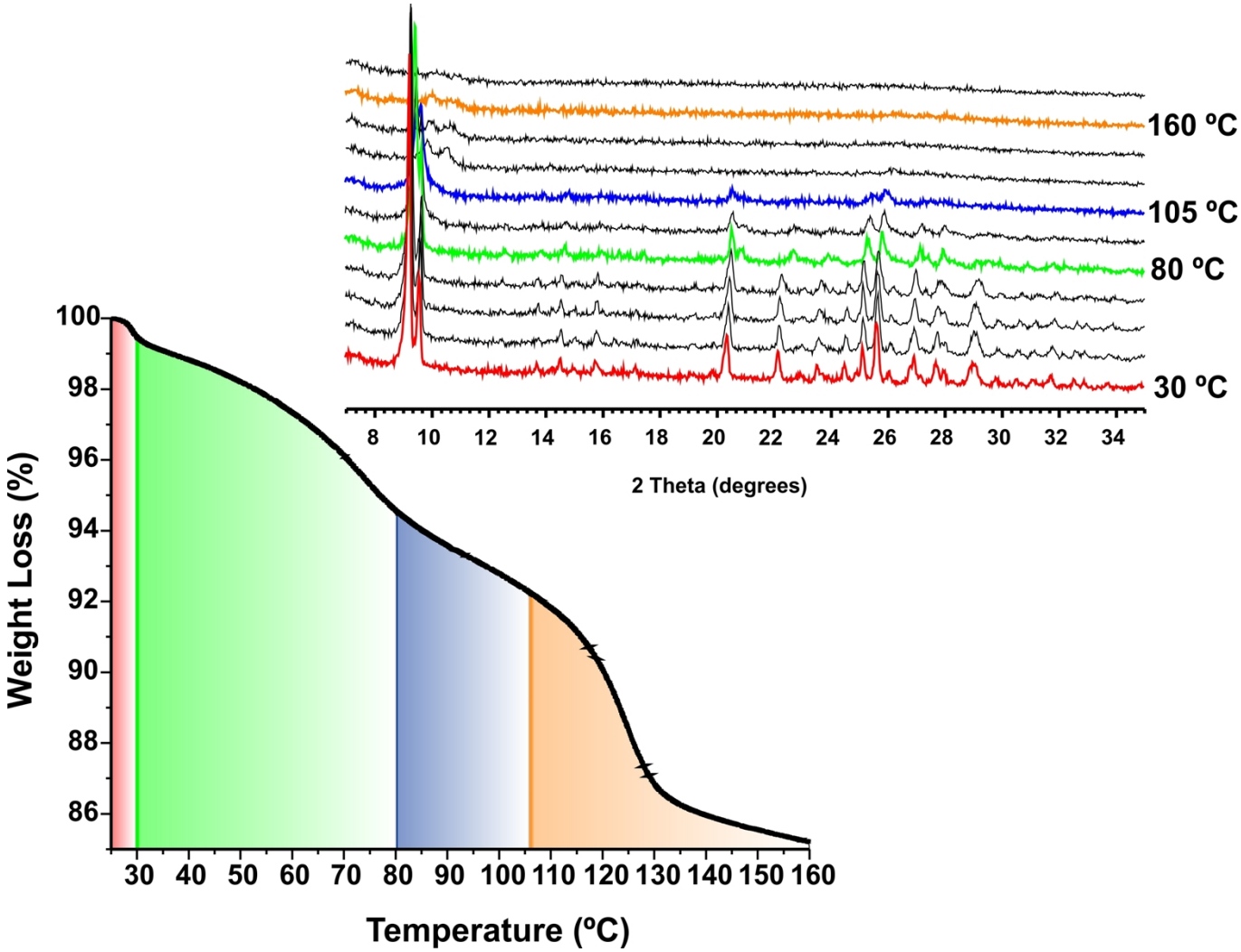

Figure S5. Correspondence between the thermogram of $[La_2(H_3nmp)_2(H_2O)_4]\cdot 4.5H_2O$ (**1mw**), collected between ambient temperature and *ca.* 160 ºC (heating rate of 1 ºC/min), with variable temperature powder X-ray diffraction studies.

The thermal stability of $[La_2(H_3nmp)_2(H_2O)_4]\cdot 4.5H_2O$ (**1h**) was investigated between ambient temperature and *ca.* 800 ºC as depicted in Figure S4. The presence of a large quantity and type of water molecules in the material prompted us to investigate the same behaviour in more detail between the ambient temperature and 160 ºC by employing a much slower heating rate (Figure S5). In addition, for this latter temperature interval the overall crystallinity and phase identification of the bulk material was also evaluated by employing *in situ* variable-temperature powder X-ray diffraction studies (VTPXRD; Figure S5 - *top*).

The material does not exhibit markedly visible and separated regions of thermal stability: transformations occur continuously between ambient temperature and *ca.* 800 ºC. Nevertheless, it is clear that the thermal decomposition of the compound can be divided into two main stages: the first, corresponding to the release of all water molecules, occurs essentially at very low temperatures; the second, continuous over the overall temperature range, corresponds to the thermal decomposition of the

organic component. For the first stage a second thermogravimetric study has been performed, with a much slower heating ramp in order to try to fully understand the process of release of the water molecules (Figure S5). Between ambient temperature and *ca.* 190 ºC, **1mw** looses approximately 14.94% of mass which agrees well with the calculated value for the liberation of all water molecules, both of crystallization and coordinated (calculated value of *ca.* 14.91%). As depicted in Figure S5 (*bottom*), the release of these water molecules occurs in three-to-four consecutive steps without the presence of any plateau. Because of this it is difficult to assign each release step to a given family of water molecules. However, due to the very low temperature at which these moieties start to be liberated (as low as ambient temperature), it is feasible to assume that most of the uncoordinated molecules are released in a first stage. A similar behaviour was observed for the materials prepared using the alternative synthetic approaches: **1h** releases *ca.* 15.91% of mass up to *ca.* 160 ºC, and **1op** *ca.* 15.44% up to a temperature of *ca.* 180 ºC (see Experimental Section and Figure S8).

Variable-temperature powder X-ray diffraction studies on **1mw** corroborate the aforementioned assumption concerning the order of release of the water molecules (Figure S5 – *top*): up to a temperature of *ca.* 90 ºC, the material retains some degree of crystallinity, strongly indicating that the released water molecules are not structurally very significant for the integrity of the 1D coordination polymer; when the coordinated water molecules start to be released, the structure collapses and the material becomes amorphous, as clearly observed for the study performed at *ca.* 160 ºC.

Upon release of all water molecules, and after the compound becomes fully amorphous, the various weight losses observed are attributed to the slow decomposition of the organic component.

2.2. Bulk 1mw *vs.* 1h *vs.* 1op

2.2.1. Powder X-ray Diffraction and SEM studies

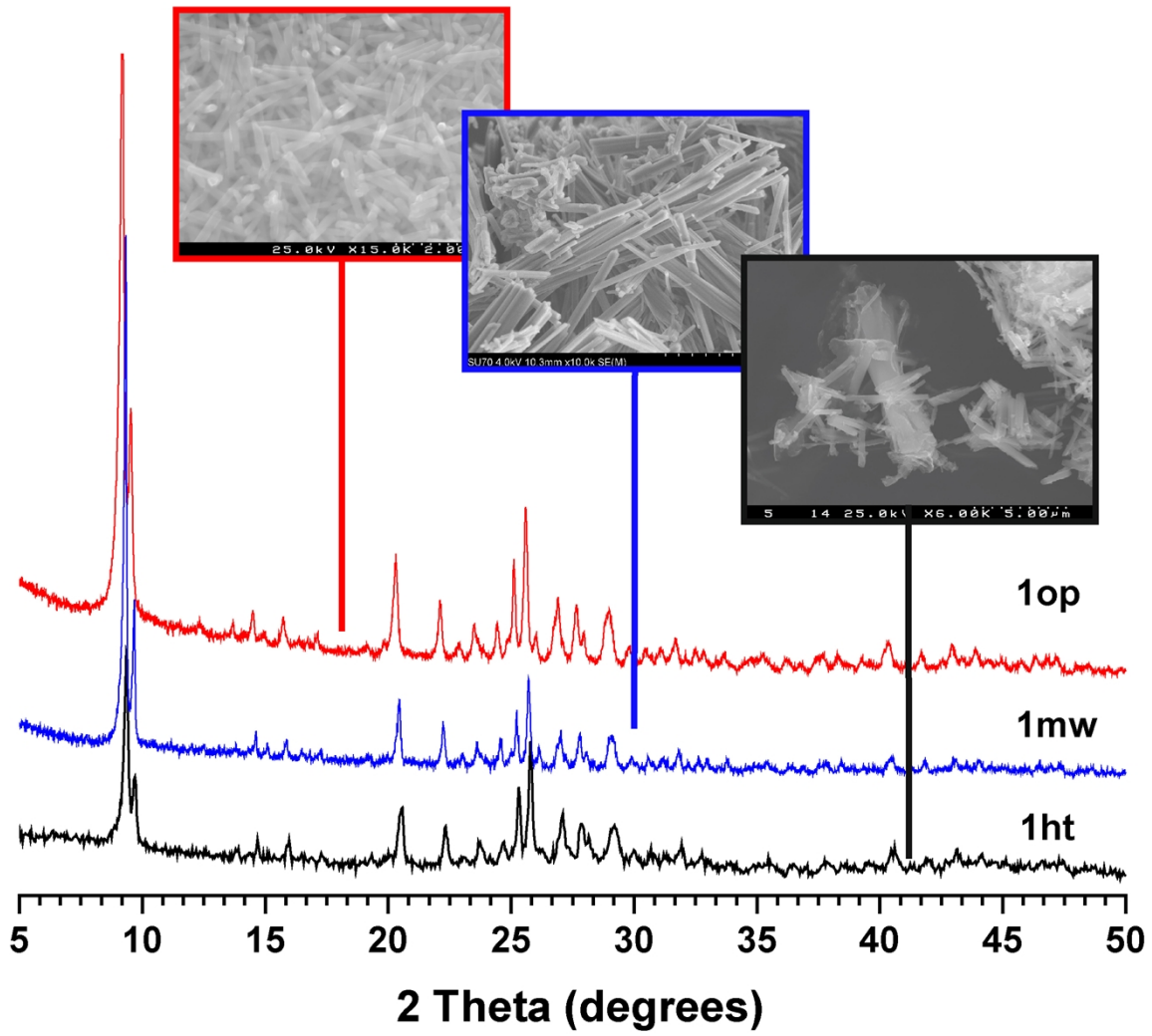

Figure S6. Comparison between the powder X-ray diffraction patterns and SEM images of the bulk $[La_2(H_3nmp)_2(H_2O)_4]\cdot 4.5H_2O$ material obtained using the three methods described in the experimental section: **1mw**, **1op** and **1h**.

2.2.2. FT-IR Spectroscopy Studies

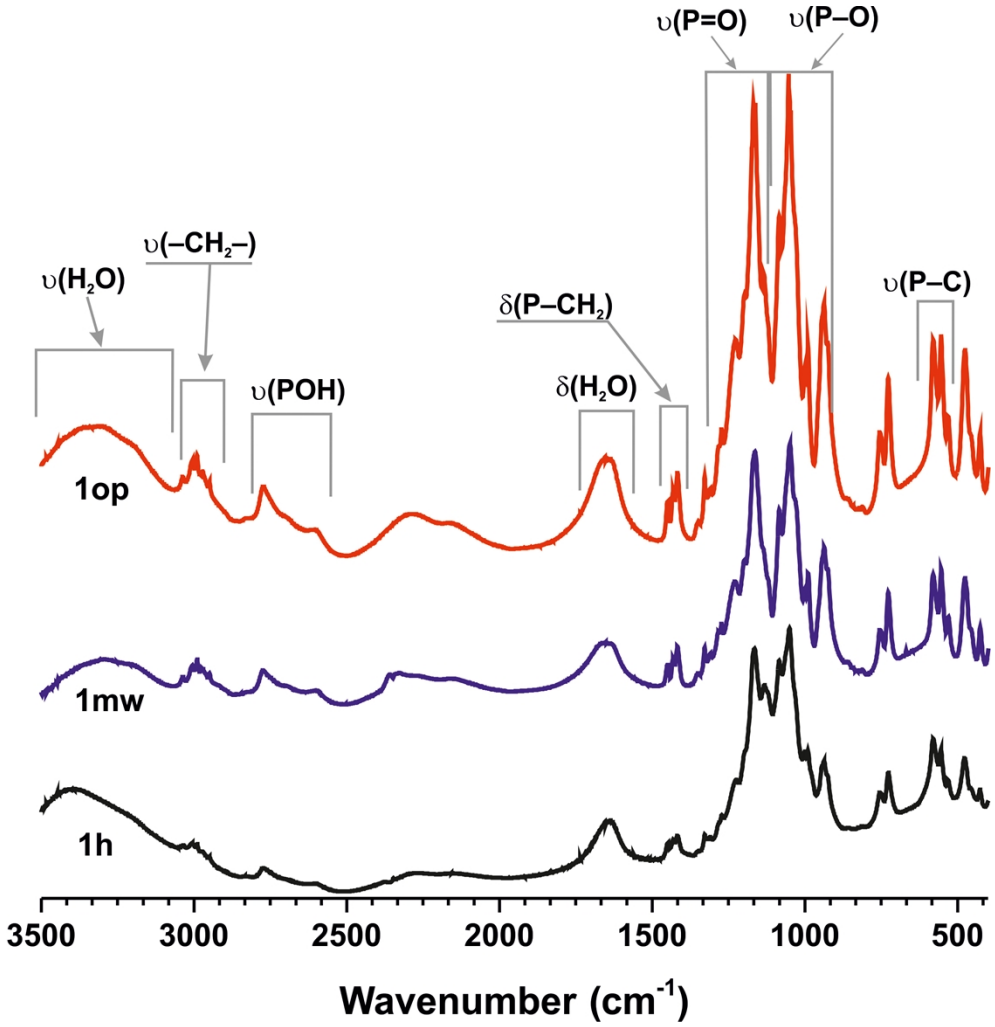

Figure S7. Comparison between the FT-IR spectra of the bulk $[La_2(H_3nmp)_2(H_2O)_4]\cdot 4.5H_2O$ materials obtained using the three methods described in the experimental section: **1mw**, **1op** and **1h**.

The FT-IR spectra of the bulk $[La_2(H_3nmp)_2(H_2O)_4]\cdot 4.5H_2O$ materials is identical for the three employed synthetic methods as depicted in Figure S7, with the most striking bands being clearly associated with the chemical moieties composing the asymmetric unit.[17] The presence of a large number and diversity of water molecules is clearly observed in the spectra, with the existence of broad bands in the *ca.* 3500-3000 cm^{-1} and 1750-1650 cm^{-1} sprectral ranges, attributed to the stretching and deformation vibrational modes of these chemical entities, respectively. The spectral region below *ca.* 1200 cm^{-1} is rich in various vibrational modes attributed to the coordinated phosphonate groups, particularly the symmetric and antisymmetric ν(P=O) modes. The presence of protonated POH groups from the organic linker is also markedly visible in the *ca.* 2850-2500 cm^{-1} spectral region, alongside with the $-CH_2-$ moieties which give rise to a number of stretching vibrational modes in the *ca.* 3050-2900 cm^{-1} spectral region.

2.2.3. Thermogravimetry

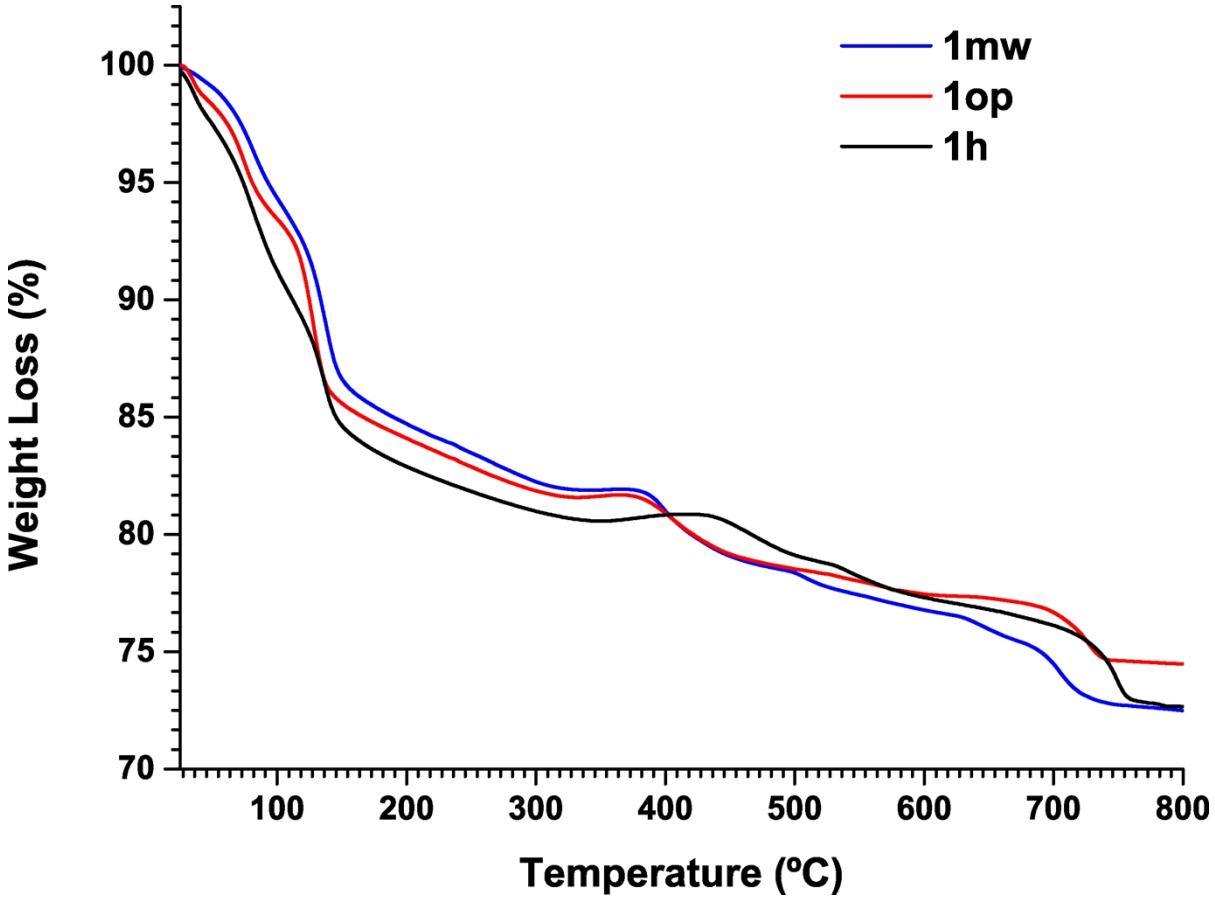

Figure S8. Comparison between the thermograms of the bulk $[La_2(H_3nmp)_2(H_2O)_4]\cdot 4.5H_2O$ materials obtained using the three methods described in the experimental section: **1mw**, **1op** and **1h**.

Thermogravimetric studies for the bulk $[La_2(H_3nmp)_2(H_2O)_4]\cdot 4.5H_2O$ material prepared using the three employed synthetic approaches show that the thermal behaviour is very similar for all compounds. The small differences observed are attributed to the effect of the distinct crystallite size as shown in Figure S6, which has some influence in the kinetics of release of the various chemical components, particularly the water molecules (both of crystallization and coordinated).

2.2.4. Crystal structure overlay

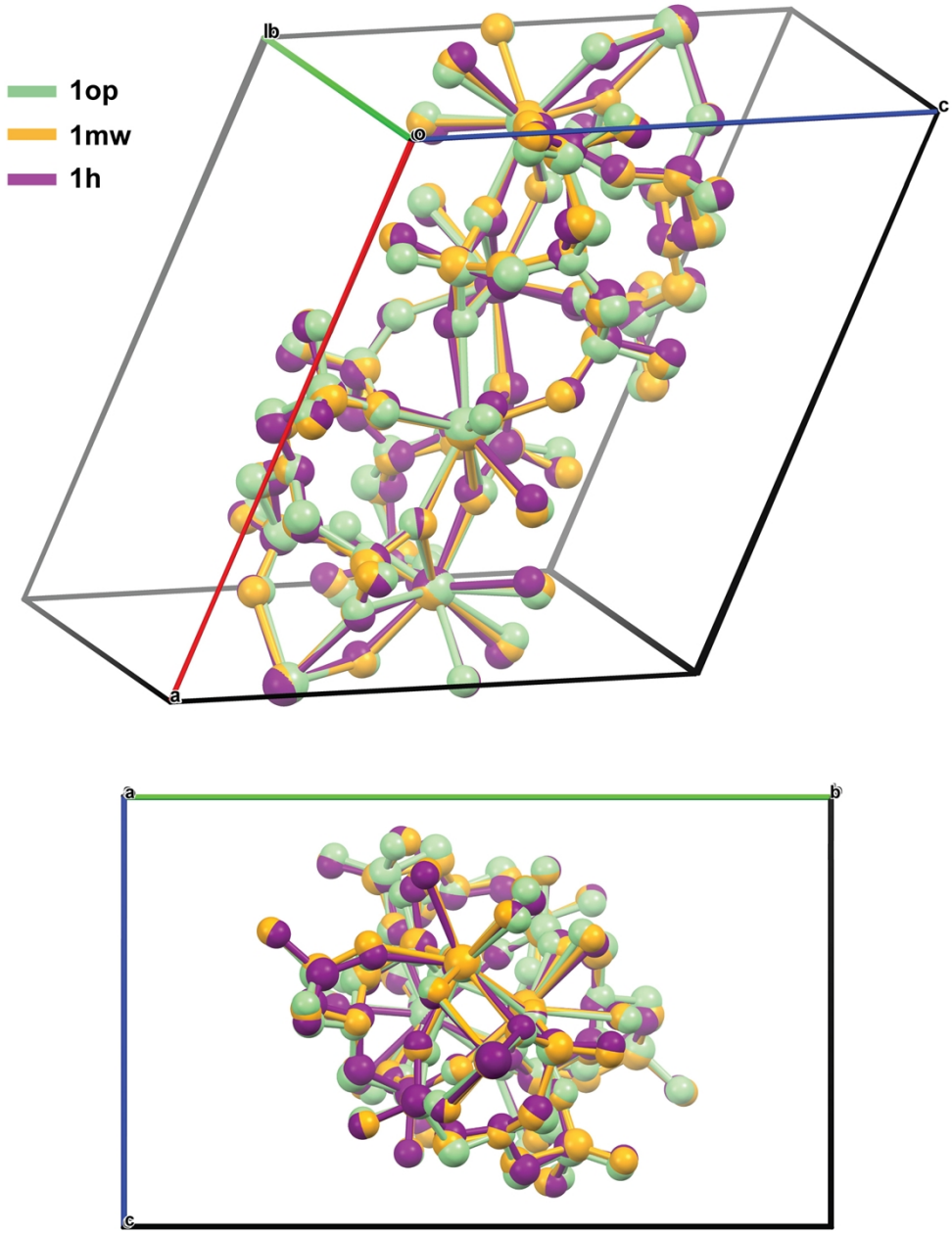

Figure S9. Unit cell and structure overlay of the $^{\infty}_{1}[La_2(H_3nmp)_2(H_2O)_4]$ one-dimensional polymers present in the crystal structure determinations of **1mw**, **1h** and **1op**. Images produced using the software package Mercury.

3. Heterogeneous Catalysis

3.1. Epoxide Ring Opening

$[La_2(H_3nmp)_2(H_2O)_4]\cdot 4.5H_2O$ (**1mw**) exhibited very high catalytic activity and excellent regioselectivity in the alcoholysis of styrene oxide (PhEtO) with methanol or ethanol (Figure S10), giving the corresponding β-alkoxy alcohol products with 100% selectivity and 99% yield at 30 min (2-methoxy-2-phenylethanol, MeOPhEtOH) and 3 h (2-ethoxy-2-phenylethanol, EtOPhEtOH), respectively (Table S5). The mechanism of the reaction can be described as a nucleophilic substitution under acidic conditions. The Brönsted acidity associated with the free phosphonate groups in **1mw** can favour the protonation of the oxygen atom of the epoxide group. This leads to favourable nucleophilic attack of the alcohol reagent at the more substituted carbon atom of the epoxide group, leading to the beta-alkoxy alcohol product. A possible reaction mechanism is hypothesized in Scheme S1. No secondary reaction products originating from the decomposition of the reagents were detected, suggesting an excellent efficiency for this catalytic system. In the absence of the catalyst, no reaction of PhEtO occurred. Noteworthy, a six-fold decrease in the amount of **1mw** from 20 to 3.3 g_1 L^{-1} led to similar outstanding catalytic results (100% MeOPhEtOH yield at 3 h reaction).

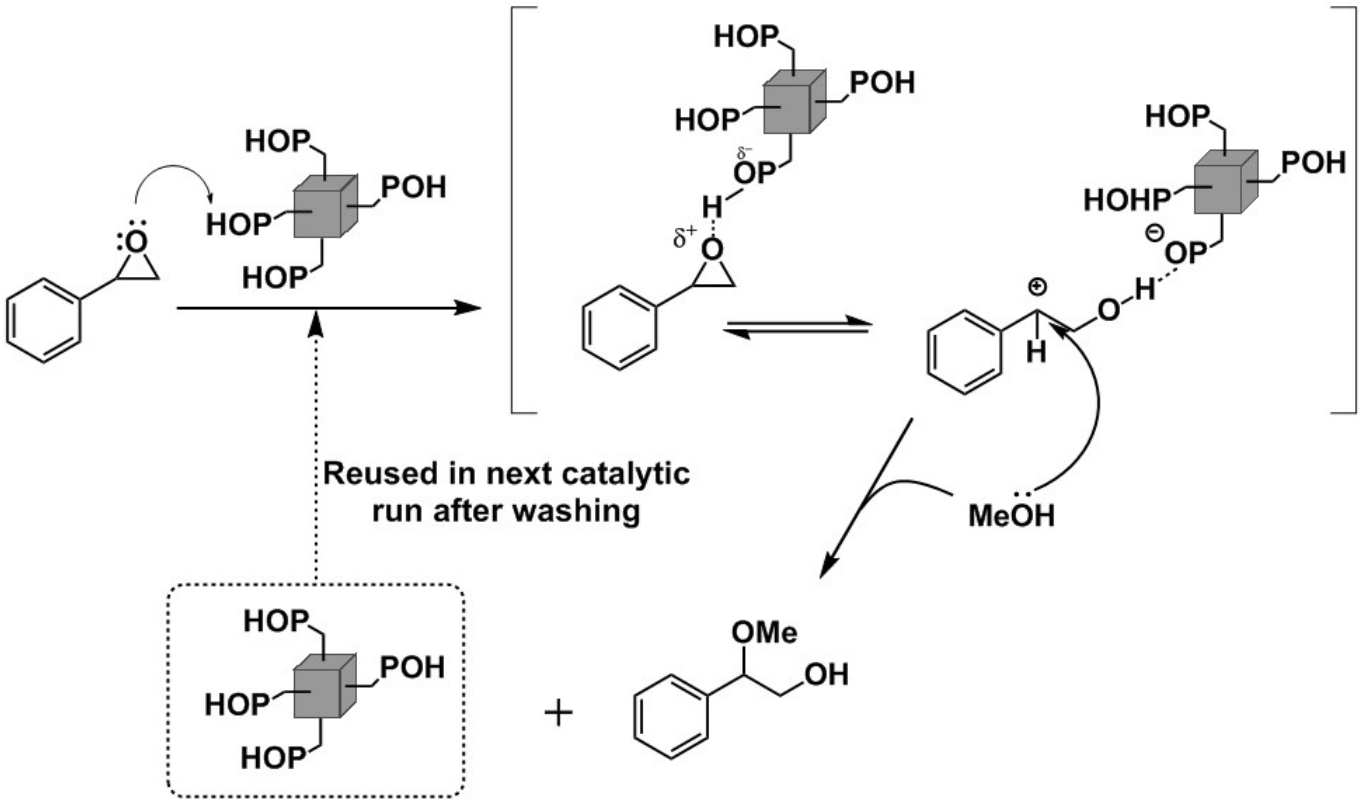

Scheme S1 - Proposed mechanism for the alcoholysis of styrene oxide (PhEtO) with methanol using **1mw** as a heterogeneous catalyst.

The reaction of PhEtO was faster with methanol than with ethanol, in good agreement with literature data for epoxide alcoholysis when MOFs are used as catalysts.[2, 18] This feature may be partly due to steric hindrance effects associated with the nucleophilic attack of the alcohol at the more hindered carbon atom of the oxirane ring. It is worth mentioning that the regio-chemical outcome of the epoxide ring opening reactions under acid or base conditions can be different: in the acid-catalysed reaction the nucleophile preferentially attacks the more substituted carbon of the oxirane ring, whereas in the base-catalysed reaction the less substituted carbon is preferred. Accordingly, the excellent regioselectivity towards the β-alkoxy alcohol product in the case of **1mw** is consistent with the acid nature of the active sites.

The hybrid material was reused in consecutive batch runs of the methanolysis of PhEtO. The solid catalyst was washed and dried under atmospheric conditions prior to reuse. The initial reaction rate decreased slightly from the first to the second run, and then remained somehow similar. Conversion was, at least, 99% in consecutive 2 h batch runs, with MeOPhEtOH selectivity being always 100%. While the crystalline structure of **1mw** was preserved, the average crystallite size decreased very slightly after the 1st run remaining relatively unchanged in subsequent runs (Figure S11). The structural integrity of the catalyst was further probed by using FT-IR spectroscopy (Figure S12).

A comparative study of the catalytic performances of the ligand (H_6nmp) and the lanthanide precursors La_2O_3 (used in equivalent molar amounts to those corresponding to 3.3 g_l L^{-1}) indicated that the catalytic reaction is strongly promoted by Brönsted acidity (Figure S13): while H_6nmp led to MeOPhEtOH as the sole product formed with 97% yield at 30 min, the reaction of PhEtO in the presence of La_2O_3 was sluggish (a maximum conversion of 3% was reached at 30 min reaction; afterwards the catalyst was deactivated). The catalytic activity of **1mw** resembles more closely that of the ligand precursor than of the lanthanide one. Hence, the high catalytic activity of **1mw** is likely due to Brönsted acid sites associated with its organic component. Similar results have been reported in the literature for the one-dimensional hybrid polymer $[La(H_4bmt)(H_5bmt)(H_2O)_2]\cdot 3H_2O$ that exhibited outstanding catalytic performance in the ring opening of styrene oxide,[19] even outperforming at that time the nano-sized commercial $[Cu_3(BTC)_2]$ MOF (well known as HKUST-1) in the same catalytic reaction.[20] Table S5 compares the catalytic results of **1mw** with those reported in the literature for various MOFs tested as catalysts in the same reaction. The catalytic performance of **1mw** stands out outperforming all other materials.

In order to effectively test which active sites are the responsible for the catalytic activity of **1mw** the material was subjected to a post-synthetic acid treatment in order to promote the formation of defect sites on the crystal surface (**1mw**-AcT). Similar high product yields were reached at 1 h of reaction for **1mw** and **1mw**-AcT (99% and 98%, respectively), albeit the initial reaction rate was lower in the latter case (dropped by a factor of *ca.* 1.6 – data not shown). These results clearly suggest that the defect sites do not

play an important catalytic role, and somewhat support that the active sites of **1mw** are Brönsted acid species.

The catalyst could be easily separated from the reaction mixture by filtration or centrifugation. The heterogeneous nature of the catalyst **1mw** was assessed using a leaching test (details given in the Experimental Section). After separating the solid catalyst from the reaction mixture at 15 min and 35 ºC, the conversion of PhEtO (*ca.* 45%) ceased to increase, indicating the absence of soluble active species and, ultimately, that **1mw** is a true heterogeneous catalyst (Figure S14). Even though the ligand precursor H_6nmp was more active than **1mw** (Figure S13), it dissolved completely in the reaction medium being, in this fashion, an homogeneous catalyst for which, in practical applications, more demanding separation and purification processes than **1mw** would be required to separate the catalyst from the target product.

3.2. Acetalization of Benzaldehyde

$[La_2(H_3nmp)_2(H_2O)_4]\cdot 4.5H_2O$ (**1mw**) was further studied as an heterogeneous acid catalyst in the acetalization of benzaldehyde (BA) with methanol at 35 ºC. The material exhibited excellent selectivity towards benzaldehyde dimethyl acetal (BADMA), which was formed as the sole product with 94% yield at 20 h reaction (Figure S15). Table S6 compares the catalytic results for **1mw** with those reported in the literature for various materials tested as solid acid catalysts in the same reaction. The catalytic performance of **1mw** compares favourably with that of other MOFs, namely $[Al_2(BDC)_3]$, [Fe(BTC)] and $[Cu_3(BTC)_2]$, as well as to other types of solid acid catalysts such as classical large-pore zeolites and mesoporous aluminosilicates (Table S6). The registered differences in catalytic activities between the various materials may be partly due to distinct acidic properties. For example, Timofeeva *et al.*[21] reported that the inclusion of electron-withdrawing NO_2-groups into the UIO-66 framework enhanced its acidity and, ultimately, the catalytic activity in the acetalization of BA with methanol.

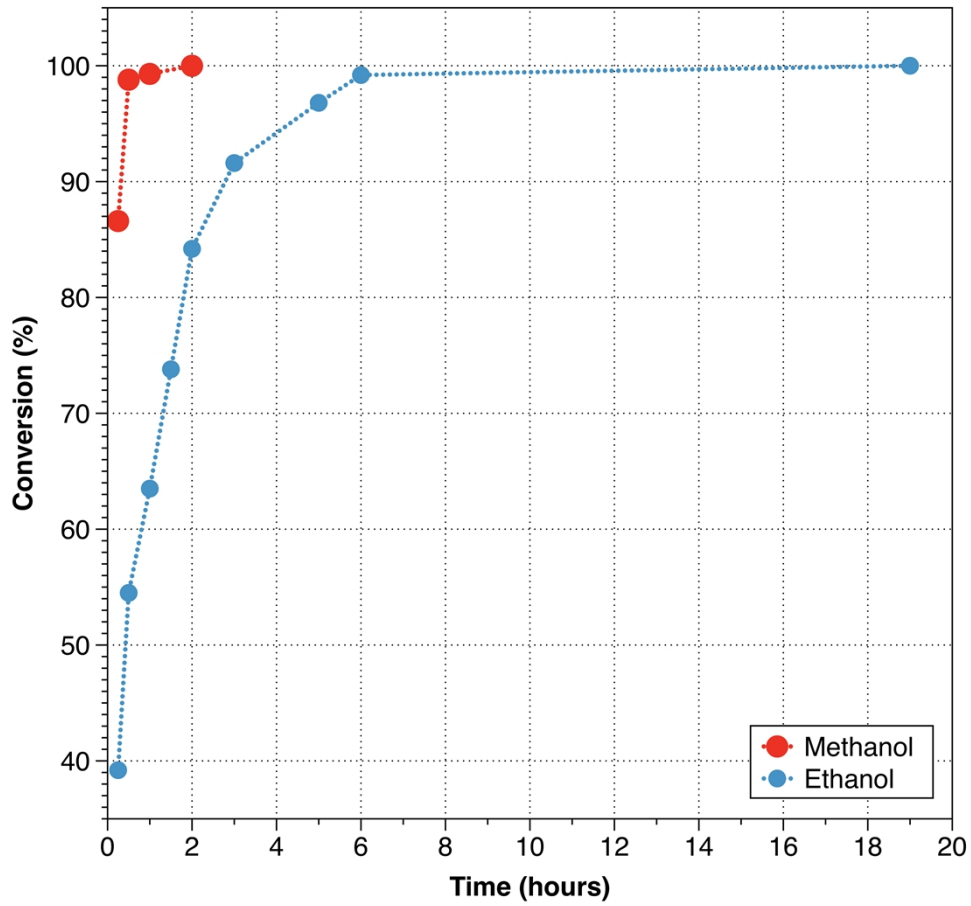

Figure S10. Conversion of styrene oxide with methanol or ethanol in the presence of $[La_2(H_3nmp)_2(H_2O)_4]\cdot 4.5H_2O$ (**1mw**) at 35 ºC (catalyst load = 20 g_1 L^{-1}). The corresponding β-alkoxy alcohol product was formed with 100% selectivity. *Please note*: dashed lines connected experimental points are only for illustrative purposes.

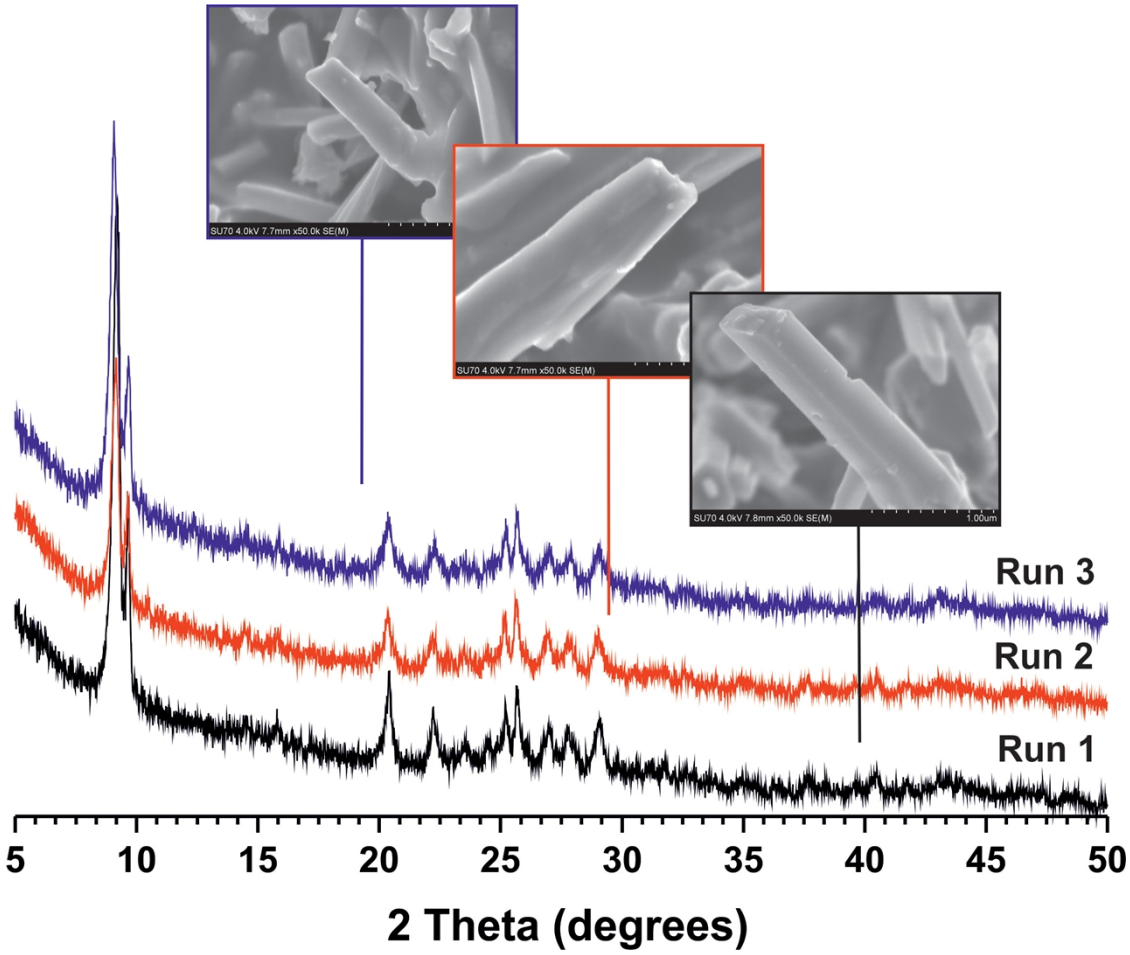

Figure S11. Powder X-ray diffraction patterns and SEM images of the bulk $[La_2(H_3nmp)_2(H_2O)_4]\cdot 4.5H_2O$ (**1mw**) catalyst used in three consecutive batch runs of styrene oxide methanolysis.

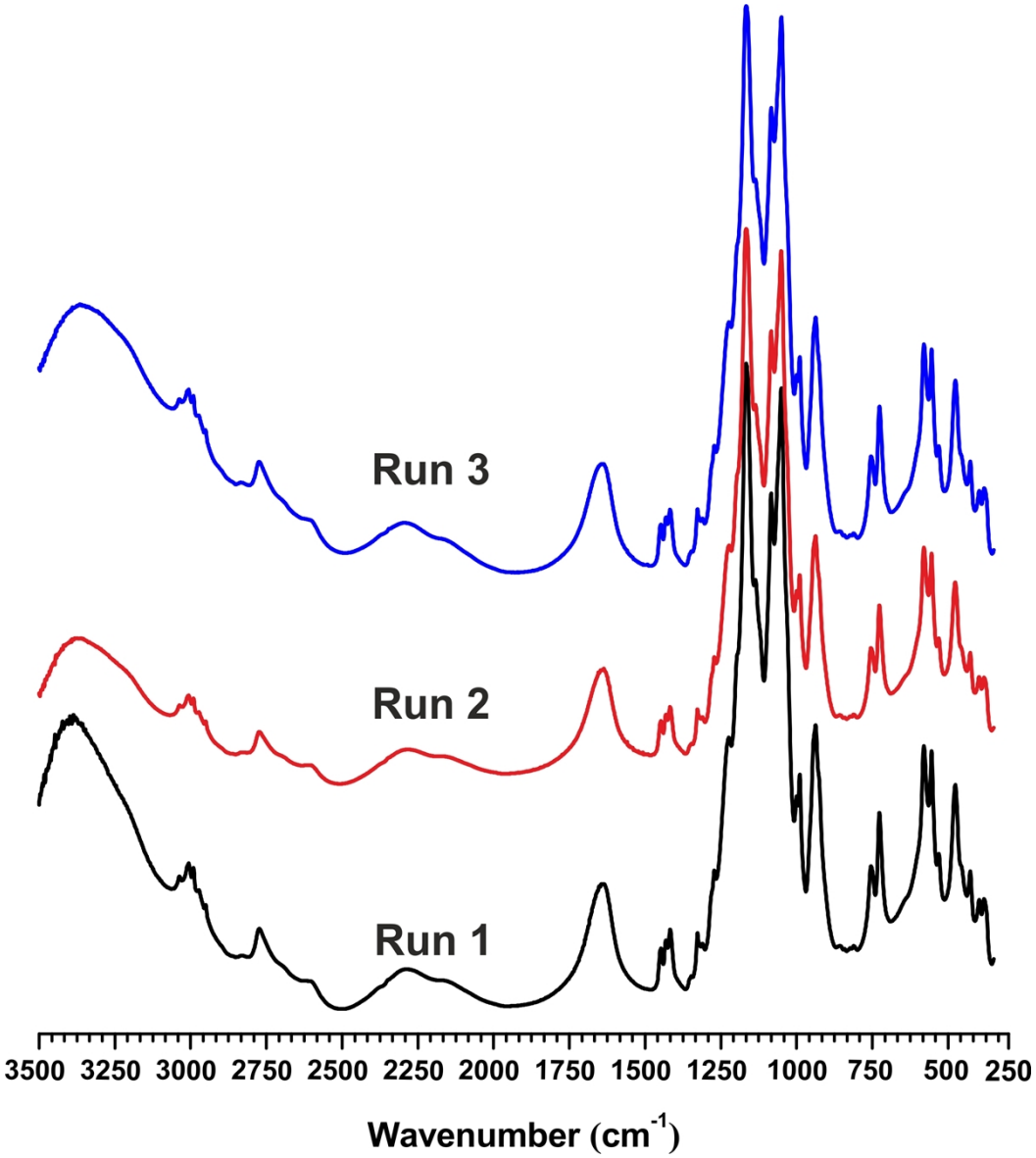

Figure S12. FT-IR spectra of the bulk $[La_2(H_3nmp)_2(H_2O)_4]\cdot 4.5H_2O$ (**1mw**) catalysts used in three consecutive batch runs of styrene oxide methanolysis.

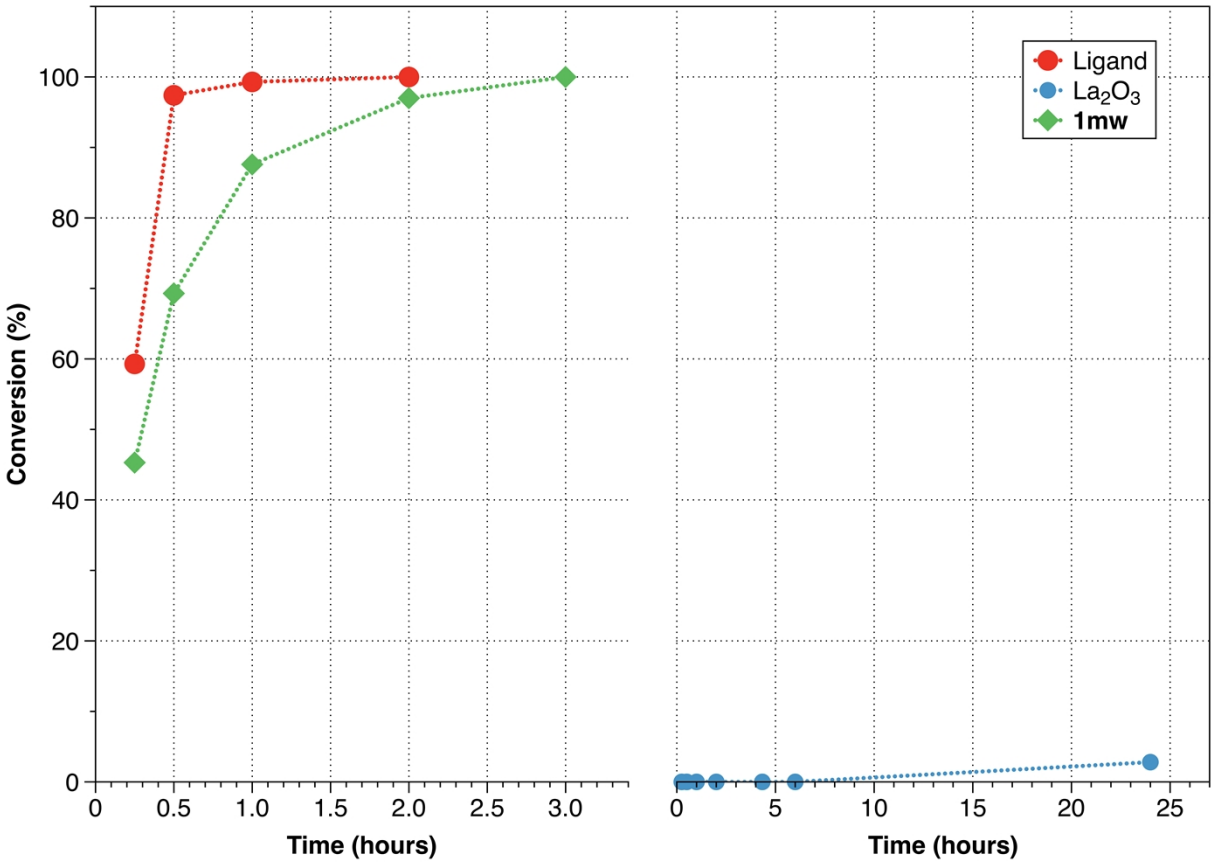

Figure S13. Conversion of styrene oxide with methanol in the presence of **1mw**, the ligand precursor H_6nmp or the lanthanide precursor (La_2O_3), at 35 ºC (catalyst load = 3.3 g_1 L^{-1}). The precursors were used in equivalent molar amounts to those corresponding to 3.3 g_1 L^{-1}. 2-Methoxy-2-phenylethanol was formed with 100% selectivity. *Please note*: dashed lines connected experimental points are only for illustrative purposes.

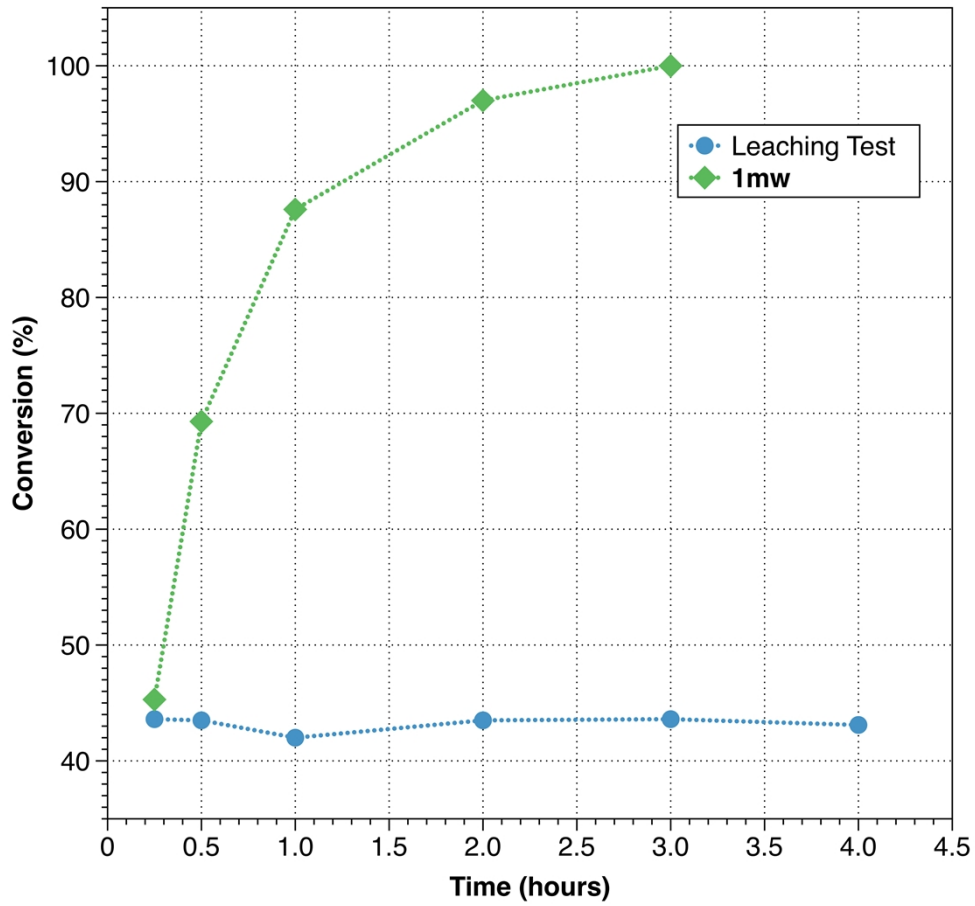

Figure S14. Leaching test carried out for **1mw** in the methanolysis of styrene oxide at 35 ºC, and comparison to the typical conditions without filtration of the catalyst (catalyst load = 3.3 g_I L^{-1}). 2-Methoxy-2-phenylethanolwas formed with 100% selectivity. *Please note*: dashed lines connected experimental points are only for illustrative purposes.

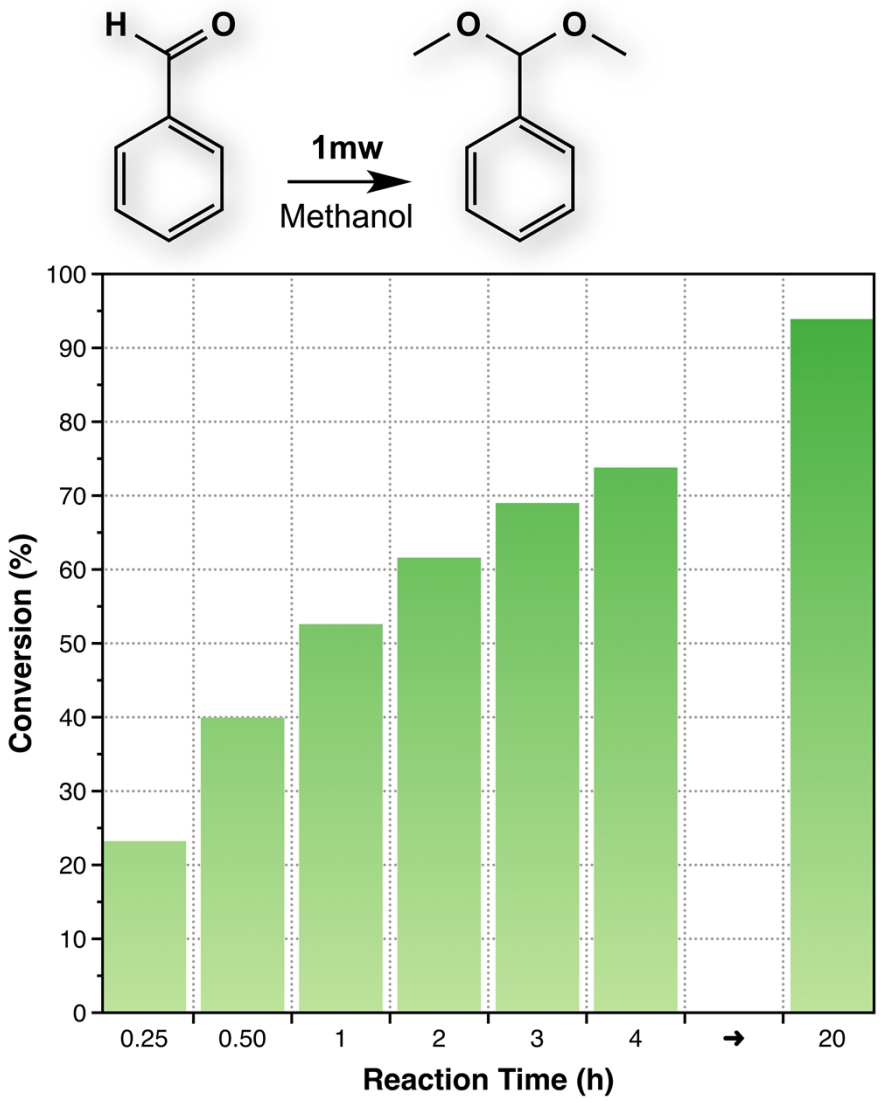

Figure S15. Conversion of benzaldehyde with methanol in the presence of **1mw** at 35 ºC (catalyst load = 20 g_1 L^{-1}). The corresponding benzaldehyde dimethyl acetal product was formed with 100% selectivity.

Table S5. Epoxide ring opening of styrene oxide (PhEtO) with methanol or ethanol, in the presence of various MOF catalysts.[a]

MOFs	Solvent	T (°C)	PhEtO (M)	Cat. (g_{cat} L^{-1})	Time	Conv. (%)	Sel. (%)	Ref.
1mw	**MeOH**	**35**	**0.40**	**20**	**15 min / 30 min**	**87 / 99**	**100**	-
1mw	**MeOH**	**35**	**0.40**	**3.3**	**30 min / 2 h**	**69 / 97**	**100**	-
1mw	**EtOH**	**35**	**0.40**	**20**	**30 min / 2 h / 6 h**	**55 / 84 / 99**	**100**	-
$[La(H_4bmt)(H_5bmt)(H_2O)_2]\cdot 3H_2O$	**MeOH**	**35**	**0.40**	**3.3**	**1 h / 6 h**	**40 / 100**	**100**	19
$[La(H_3nmp)]$	MeOH	40	0.42	17.4	24 h / 48 h / 72 h	40 / 77 / 100	100	2
$[La_2(H_3bmt)_2(H_2O)_2]\cdot H_2O$	MeOH	55	0.41	20	4 h / 24 h	10 / 80	100	22
$[Ce_2(pydc)_3(H_2O)_2]$	MeOH	55	0.41	16.3	24 h / 48 h	73 / 77	100	23
$[Ce_2(pydc)_3(H_2O)_2]$	MeOH	55	0.41	3.3	24 h / 48 h	49 / 54	100	23
$[Cu(bpy)(H_2O)_2(BF_4)_2(bpy)]$	MeOH	rt	0.25	12.9	2 h	93	100	18
$[Cu_3(BTC)_2]$ (HKUST-1)	MeOH	40	0.17	6.7	2.5 h	90	100	20
$[Cu_3(BTC)_2]$ (HKUST-1)	MeOH	40	0.40	10	10 min / 1 h	25 / 93	98/95	24
[Fe(BTC)]	MeOH	40	0.40	10	20 min / 1 h	69 / >99	97/94	25
[Fe(BTC)]	EtOH	40	0.40	10	1 h / 24 h	14/35	>95	25
$[Al_2(BDC)_3]$	MeOH	40	0.40	10	30 min / 1 h	21/67	98/96	25
MIL-101(H_2O)	MeOH	40	0.13	5	20 min	22	>99	24
MIL-101(HPW)	MeOH	40	0.13	5	20 min	99	>99	24
MIL-53(Al)-AMMal	CD_3OD	25	0.20	[c]	48 h	100	100	26

[a] The experimental conditions which were used are indicated for comparison: solvent, reaction temperature (T; rt = ambient temperature), initial molar concentration of PhEtO, catalyst load (Cat.) and reaction time. The catalytic results are reported as conversion of PhEtO (Conv.) and selectivity towards the β-alkoxy alcohol product (Sel.; when a single value of Sel. is indicated it indicates that it was constant with time).
[b] The abbreviations of the names of the MOFs are the same as those used in the original publications.
[c] The amount of MOF used was *ca.* 0.04 mol (based on free carboxylate groups) per litre of alcohol.

Table S6. Acetalization of benzaldehyde (BA) with methanol in the presence of solid acid catalysts.[a]

Solid catalyst [b]	T (ºC)	BA (M)	Cat. (g_{cat} L^{-1})	Time (h)	Conv. (%)	Sel. (%)	Ref.
UIO-66-NO_2	**30**	**0.31**	**16.7**	**4**	**100**	**100**	21
1mw	**35**	**0.40**	**20**	**4/20**	**74/94**	**100**	-
UIO-66-NH_2	30	0.31	16.7	4/18	20/81	100	21
[Cu_3(BTC)$_2$]	rt	0.31	16.7	24	88	100	27
[Cu_3(BTC)$_2$]	rt	3.13	16.7	48	66	98	27
[Cu_3(BTC)$_2$]	rt	0.33	33.3	24	94	100	27
[Al_2(BDC)$_3$]	rt	0.31	16.7	24	66	100	27
[Fe(BTC)]	rt	0.31	16.7	24	71	100	27
Bentonite	rt	0.33	33.3	8	5	100	27
NaY	rt	0.33	33.3	8	10	100	27
USY-500	rt	0.33	33.3	24	63	100	27
Zeolite Beta	rt	0.33	33.3	24	69	100	27
MIL101/PTA	25	0.47	1.5	24	95	100	28
PTA	25	0.47	1.5	24	93	100	28
MIL-101	25	0.47	1.5	24	80	100	28
MIL-100(Fe)	40	0.59	2	21	69	100	29
[Fe(BTC)]	40	0.59	1.8	21	84	100	29
Al-MCM-41	50	0.33	6.7	5	56	96	30
Ce^{3+}-Montmorillonite	rt	2.47	5	10	91	100	31
H-Y	rt	2.47	5	10	32	100	31
Ce-H-Y	rt	2.47	5	10	70	100	31
γ-Al_2O_3	rt	2.47	5	10	4	100	31
SiO_2	rt	2.47	5	10	0	100	31

[a] Experimental conditions: T = reaction temperature (*please note*: rt = ambient temperature); BA = initial molar concentration of BA; Cat. = catalyst load; reaction time. The catalytic results are reported as conversion of BA (Conv.) and selectivity towards BA-acetal (Sel.).
[b] The abbreviations of the names of the solid catalysts are the same as those used in the original publications.

4. Transformation Studies

$[La_2(H_3nmp)_2(H_2O)_4]\cdot 4.5H_2O$ (**1mw**) can be transformed at 100 ºC into two different layered materials reported previously by our group (Figure S16): $[La(H_3nmp)]\cdot 1.5H_2O$ (**2**)[1] and $[La(H_3nmp)]$ (**3**).[2] Using one-pot conditions, **2** is always isolated as a pure phase after 24 h (Figure S17). The same occurs when a hydrothermal approach is employed in conjunction with a very slow cooling of the reaction vessels up to the ambient temperature (Figure S18). If instead the vessels are quenched in cold water, a mixture of both **2** and **3** is isolated, with the latter material being the predominant phase (Figure S19). Figure S16 summarizes the reaction conditions employed for the transformation tests and the phases that are obtained in each situation, while Figures S17 to S19 depict the powder X-ray diffraction patterns of the transformed phases compared with simulations for the two previously reported layered materials. Currently, we do not have any evidence for the real mechanism in which these transformations occur. Even though during the one-pot synthesis no complete dissolution of **1mw** was observed, the need of addition of acid to all reactions might ultimately indicate that the primary building units may, indeed, undergo dissolution in a first stage and only then be used to produce compounds **2** and **3**.

As described in the main paper, the two crystallographically independent La^{3+} coordination environments composing **1mw** share several similarities. Particularly, both environments comprise two coordinated water molecules that could easily be displaced in order to promote polymerization into compounds **2** and **3**. Indeed, as shown in Figure S16, the $_\infty^1[La_2(H_3nmp)_2(H_2O)_4]$ polymer can be topologically envisaged as a zigzag chain of La^{3+} cations with intermetallic distances oscillating between 4.25 and 4.36 Å. A close inspection of the layers present in $[La(H_3nmp)]\cdot 1.5H_2O$[1] and $[La(H_3nmp)]$,[2] both with a (4,4) topology, reveals that their core is simply assembled by the lanthanide cation and one phosphonate group, with small differences in the connectivities as shown in Figure S16. In the case of compound **2**, a clear zigzag chain with intermetallic distance of 4.24 Å strongly resembles the connectivity present in **1mw**. It is, thus, not surprising to observe that this material is easily obtained under all methods employed for the transformation tests, being readily isolated as a pure phase. The core layer of compound **3** is significantly more distinct implying a strong rearrangement of the connectivity of the phosphonate group (the intermetallic distances are, for example, significantly different from those present in **1mw**). In this context, one can easily understand how the transformation requires a longer reaction time (48 h) and a drastic quench of the temperature of the reaction vessel.

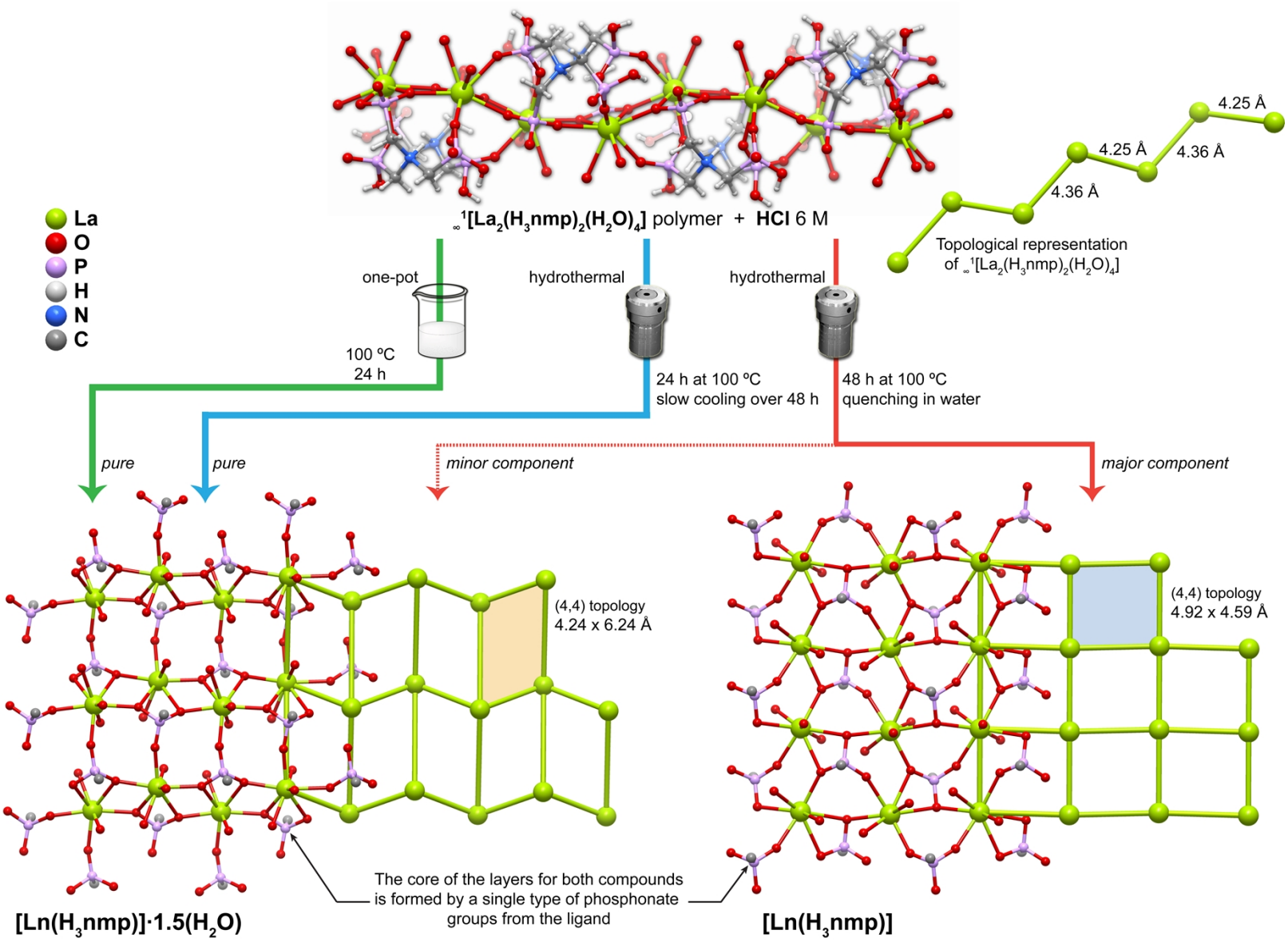

Figure S16. Conversion of [La$_2$(H$_3$nmp)$_2$(H$_2$O)$_4$]·4.5H$_2$O (**1mw**) into the layered [La(H$_3$nmp)]·1.5H$_2$O (**2**)[1] and [La(H$_3$nmp)] (**3**)[2] materials using hydrothermal and one-pot synthetic conditions.

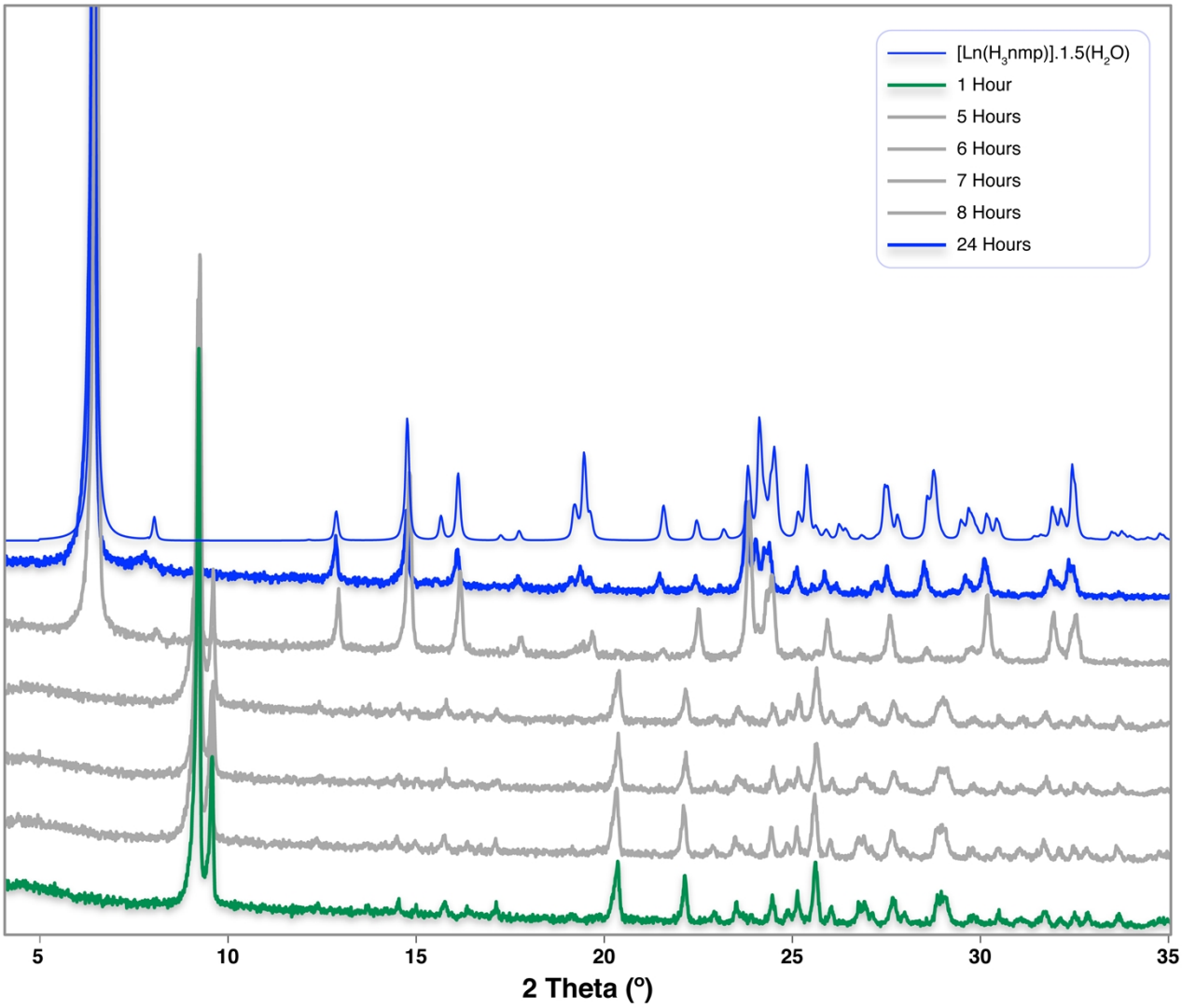

Figure S17. Conversion of $[La_2(H_3nmp)_2(H_2O)_4]\cdot 4.5H_2O$ (**1mw**) into the layered $[La(H_3nmp)]\cdot 1.5H_2O$ (**2**) material using one-pot conditions (100 ºC over 24 h).

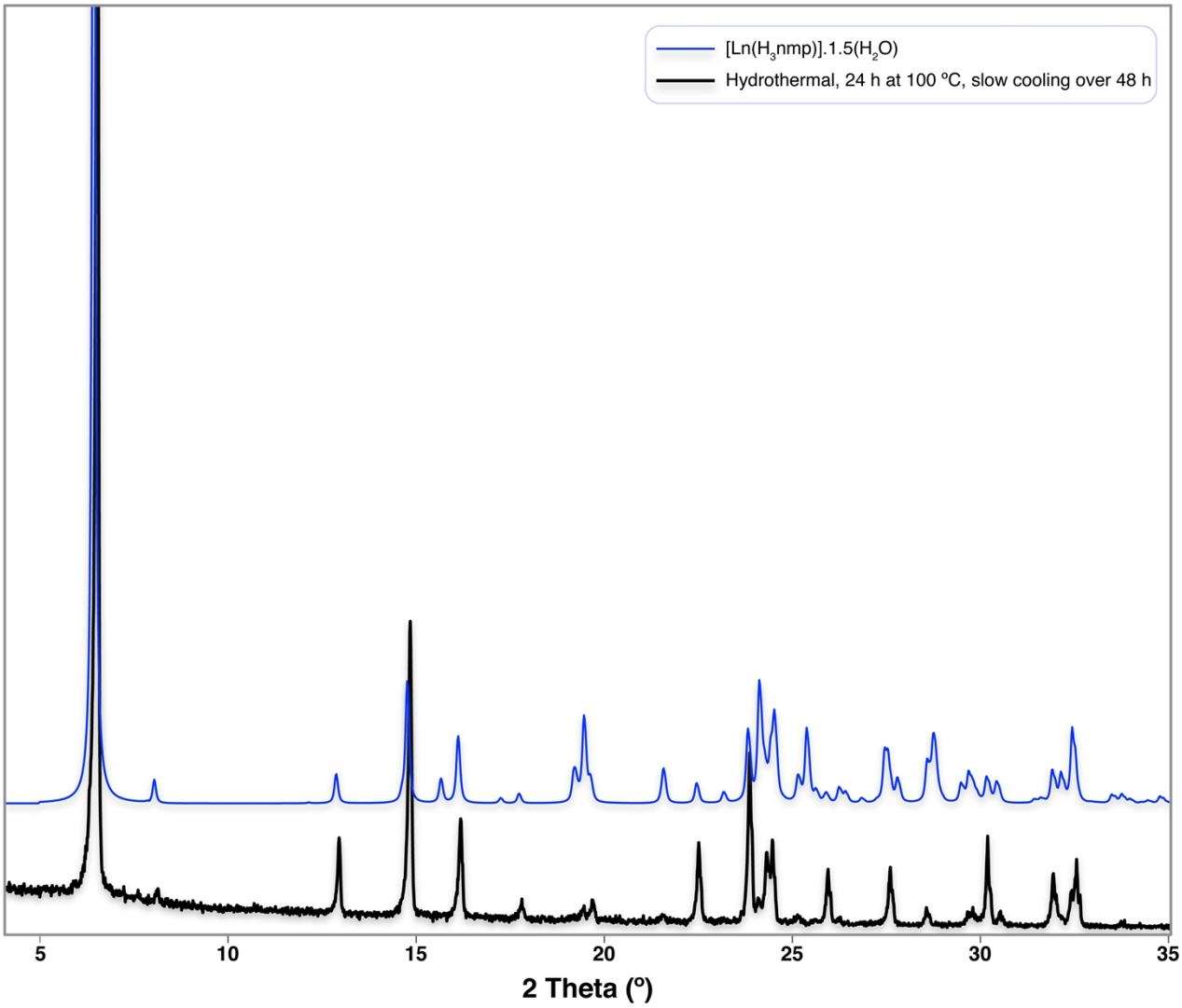

Figure S18. Conversion of $[La_2(H_3nmp)_2(H_2O)_4]\cdot 4.5H_2O$ (**1mw**) into the layered $[La(H_3nmp)]\cdot 1.5H_2O$ (**2**) material using hydrothermal conditions (100 ºC over 24 h, with slow cooling to ambient temperature over a period of 48 h).

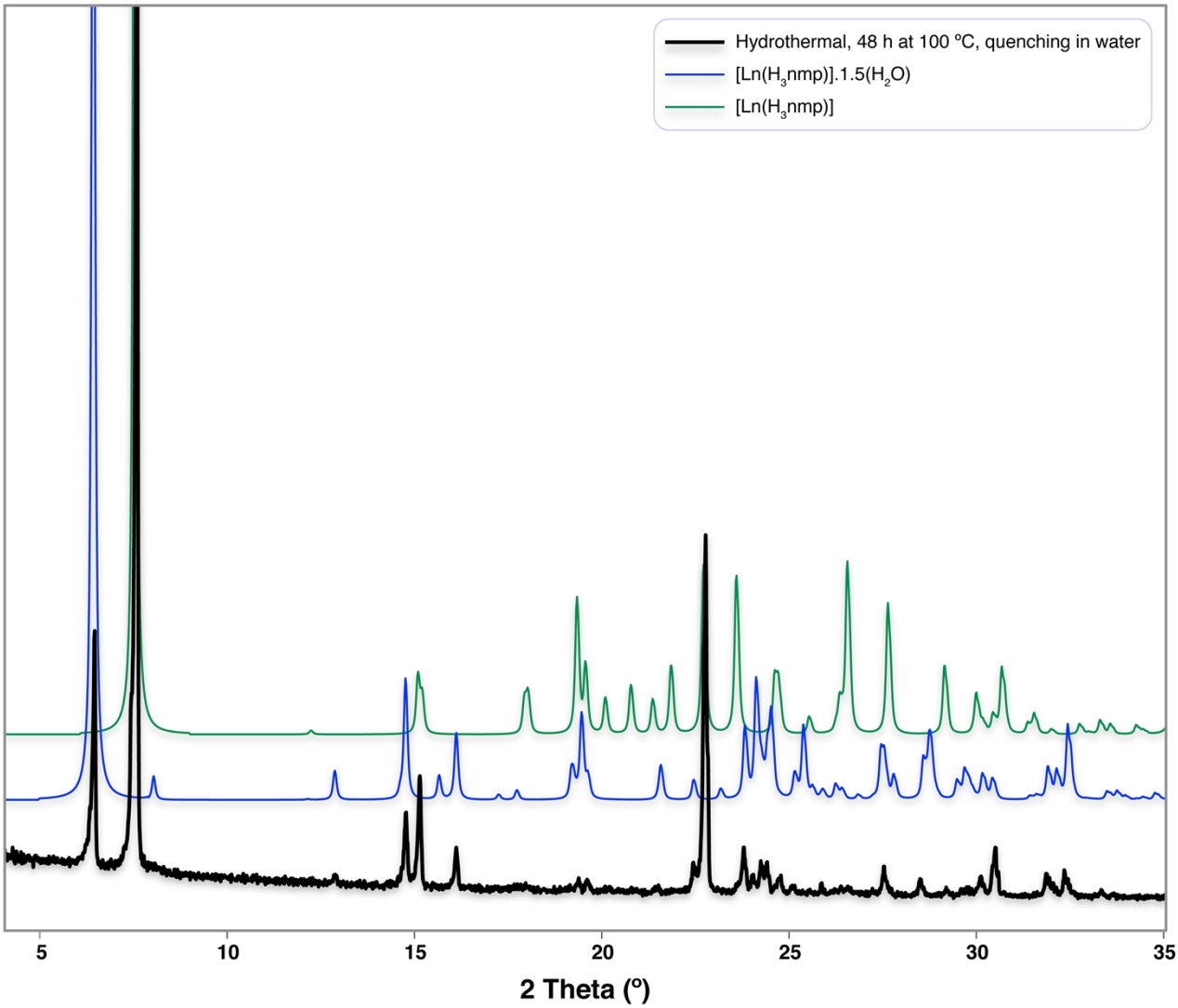

Figure S19. Conversion of $[La_2(H_3nmp)_2(H_2O)_4]\cdot 4.5H_2O$ (**1mw**) into a mixture of layered $[La(H_3nmp)]\cdot 1.5H_2O$ (**2**) and $[La(H_3nmp)]$ (**3**) materials using hydrothermal conditions (100 ºC over 48 h with a rapid quenching of the reaction vessels in cold water).

5. References

1. L. Cunha-Silva, L. Mafra, D. Ananias, L. D. Carlos, J. Rocha and F. A. A. Paz, *Chem. Mater.*, 2007, **19**, 3527-3538.
2. P. Silva, F. Vieira, A. C. Gomes, D. Ananias, J. A. Fernandes, S. M. Bruno, R. Soares, A. A. Valente, J. Rocha and F. A. A. Paz, *J. Am. Chem. Soc.*, 2011, **133**, 15120-15138.
3. T. Kottke and D. Stalke, *J. Appl. Crystallogr.*, 1993, **26**, 615-619.
4. APEX2, *Data Collection Software Version 2012.4, Bruker AXS, Delft, The Netherlands*, 2012.
5. A. A. Coelho, *J. Appl. Crystallogr.*, 2003, **36**, 86-95.
6. SAINT+, *Data Integration Engine v. 8.27b*©, 1997-2012, Bruker AXS, Madison, Wisconsin, USA.
7. G. M. Sheldrick, *SADABS 2012/1, Bruker AXS Area Detector Scaling and Absorption Correction* 2012, Bruker AXS, Madison, Wisconsin, USA.
8. G. M. Sheldrick, *SHELXT-2014, Program for Crystal Structure Solution, University of Göttingen*, 2014.
9. (a) G. M. Sheldrick, *Acta Cryst. A*, 2008, **64**, 112-122; (b) G. M. Sheldrick, *SHELXL Version 2014, Program for Crystal Structure Refinement, University of Göttingen*, 2014.
10. C. B. Hübschle, G. M. Sheldrick and B. Dittric, *J. Appl. Crystallogr.*, 2011, **44**, 1281-1284.
11. K. Brandenburg, *DIAMOND, Version 4.0.0. Crystal Impact GbR, Bonn, Germany*, 1997-2014.
12. (a) A. N. Fitch, in *European Powder Diffraction: EPDIC IV, Pts 1 and 2*, Transtec Publications Ltd, Zurich-Uetikon, 1996, vol. 228, pp. 219-221; (b) A. N. Fitch, *Journal of Research of the National Institute of Standards and Technology*, 2004, **109**, 133-142.
13. H. M. Rietveld, *J. Appl. Crystallogr.*, 1969, **2**, 65-71.
14. A. Coelho, *Topas Academic, Version 5.0, Coelho Software, Brisbane*, 2013.
15. R. W. Cheary and A. Coelho, *J. Appl. Crystallogr.*, 1992, **25**, 109-121.
16. (a) W. A. Dollase, *J. Appl. Crystallogr.*, 1986, **19**, 267-272; (b) A. March, *Zeitschrift für Kristallographie*, 1932, **81**, 285-297.
17. G. Socrates, *Infrared Characteristic Group Frequencies - Tables and Charts*, 2nd edn., John Wiley & Sons Ltd, Baffins Lane, Chichester, 1994.
18. D. M. Jiang, A. Urakawa, M. Yulikov, T. Mallat, G. Jeschke and A. Baiker, *Chem.-Eur. J.*, 2009, **15**, 12255-12262.
19. S. M. F. Vilela, A. D. G. Firmino, R. F. Mendes, J. A. Fernandes, D. Ananias, A. A. Valente, H. Ott, L. D. Carlos, J. Rocha, J. P. C. Tome and F. A. Almeida Paz, *Chem. Commun.*, 2013, **49**, 6400-6402.
20. L. H. Wee, M. R. Lohe, N. Janssens, S. Kaskel and J. A. Martens, *J. Mater. Chem.*, 2012, **22**, 13742-13746.

21. M. N. Timofeeva, V. N. Panchenko, J. W. Jun, Z. Hasan, M. M. Matrosova and S. H. Jhung, *Appl. Catal. A-Gen.*, 2014, **471**, 91-97.
22. S. M. F. Vilela, D. Ananias, A. C. Gomes, A. A. Valente, L. D. Carlos, J. A. S. Cavaleiro, J. Rocha, J. P. C. Tomé and F. A. A. Paz, *J. Mater. Chem.*, 2012, **22**, 18354-18371.
23. P. Silva, D. Ananias, S. M. Bruno, A. A. Valente, L. D. Carlos, J. Rocha and F. A. Almeida Paz, *Eur. J. Inorg. Chem.*, 2013, **2013**, 5576-5591.
24. L. H. Wee, F. Bonino, C. Lamberti, S. Bordiga and J. A. Martens, *Green Chem.*, 2014, **16**, 1351-1357.
25. A. Dhakshinamoorthy, M. Alvaro and H. Garcia, *Chem.-Eur. J.*, 2010, **16**, 8530-8536.
26. S. J. Garibay, Z. Wang and S. M. Cohen, *Inorg. Chem.*, 2010, **49**, 8086-8091.
27. A. Dhakshinamoorthy, M. Alvaro and H. Garcia, *Adv. Synth. Catal.*, 2010, **352**, 3022-3030.
28. L. Bromberg and T. A. Hatton, *ACS Appl. Mater. Interfaces*, 2011, **3**, 4756-4764.
29. A. Dhakshinamoorthy, M. Alvaro, P. Horcajada, E. Gibson, M. Vishnuvarthan, A. Vimont, J.-M. Grenèche, C. Serre, M. Daturi and H. Garcia, *ACS Catalysis*, 2012, **2**, 2060-2065.
30. S. Ajaikumar and A. Pandurangan, *J. Mol. Catal. A: Chem.*, 2008, **290**, 35-43.
31. B. Thomas, V. G. Ramu, S. Gopinath, J. George, M. Kurian, G. Laurent, G. L. Drisko and S. Sugunan, *Appl. Clay Sci.*, 2011, **53**, 227-235.